buildings

MDPI

Article

Dynamic Response and Stiffness Degradation of a Nominally Fixed Ultra-High-Performance Fiber-Reinforced Concrete Plate Under Cumulative Impact Loading: An Experimental and Numerical Study

Yuanye He [1,2], Esmaeel Esmaeeli [3,*], Marios Soutsos [4], Jian-Fei Chen [5] and Alipujiang Jierula [1,2]

1 College of Civil Engineering and Architecture, Xinjiang University, Urumqi 830046, China; yuanye.he@xju.edu.cn (Y.H.); alpj@xju.edu.cn (A.J.)
2 Xinjiang Key Laboratory of Building Structure and Earthquake Resistance, Xinjiang University, Urumqi 830046, China
3 Department of Engineering, Brunel University of London, Uxbridge UB8 3PH, UK
4 School of Natural and Built Environment, Queen's University Belfast, Belfast BT9 5AG, UK; m.soutsos@qub.ac.uk
5 Department of Ocean Science and Engineering, Southern University of Science and Technology, Shenzhen 518055, China; chenjf3@sustech.edu.cn
* Correspondence: esmaeel.esmaeeli@brunel.ac.uk

Abstract

The performance of ultra-high-performance fiber-reinforced concrete (UHPFRC) under repeated low-velocity impacts, particularly in the context of nominally fixed boundaries relevant to protective structures, remains underexplored. In practice, protective components made of UHPFRC, such as falling object barriers and vehicle parapet systems, are exposed to foreseeable repeated low-velocity impacts; however, no standardized design provisions or residual capacity assessment methods exist for such members, particularly under nominally fixed boundary conditions. This study presents an integrated experimental and numerical investigation into the progressive damage and failure mechanisms of a 50 mm thick UHPFRC plate with nominally fixed (bolted clamping) boundaries subjected to sequential low-velocity impacts. A custom drop-weight test setup was used for impact loading, while high-speed 3D digital image correlation (3D-DIC) captured the quarter-field transient kinematics, which were reconstructed back to the full field based on verified test symmetry and complemented by traditional accelerometer and strain gauge measurements. The results demonstrate a distinct progression of damage. Initial low-energy impacts (196 J/drop) caused negligible damage, highlighting the material's tolerance. Subsequent higher-energy impacts induced a transition from flexural cracking to a combined flexural–punching shear failure mode. The model-assisted nominal secant stiffness indicator decreased by 5.3% over the repeated 0.5 m drops and fell by 50.8% after the 2.0 m drop, quantifying the transition in structural behavior. A finite element (FE) model, incorporating the concrete damaged plasticity (CDP) model with an energy-based degradation law, was developed and evaluated against the experimental data. This model replicated both the quantitative dynamic responses (with model-to-test ratios of peak acceleration, strain, and displacement between 0.86 and 1.30 across three energy levels) and the qualitative damage evolution. The model thus evaluated enabled a model-derived reconstruction of the critical impact force–time history, revealing the evolution of structural degradation toward the exhaustion of the plate's global flexural resistance and the transition to a punching shear mechanism.

Academic Editor: Antonio Caggiano

Received: 3 July 2026
Revised: 10 August 2026
Accepted: 14 August 2026
Published: 19 August 2026

 https://doi.org/10.3390/buildings16163300

Keywords: ultra-high-performance fiber-reinforced concrete (UHPFRC) plate; impact behavior; fixed support; 3D digital image correlation; concrete damaged plasticity model; low-velocity impact

1. Introduction

High deformation rates can occur in civil infrastructure under various conditions, ranging from collisions with heavy objects to natural and manmade disasters [1]. Structures should be designed to withstand high strain rates under such circumstances, with only limited damage, to ensure the protection of human life and communal property [2].

Enhancing the impact resistance of structures can be achieved at the structural and/or material level. Structural strategies [3], such as increasing reinforcement and the structural dimensions [4] or external strengthening, e.g., externally bonding fiber-reinforced polymer (FRP) composites [5,6], have been proven to be effective in mitigating the effect of impact loads on reinforced concrete (RC) structures. However, concrete spalling and scabbing can also cause damage, and this cannot be prevented because of concrete's brittleness and insufficient energy absorption capacity. Therefore, improving concrete's ductility and energy absorption capacity, e.g., by mixing short discrete fibers, has attracted researchers' attention [7–9]. The role of steel fibers in enhancing member stiffness and capacity has also been demonstrated for other configurations [10]. Ultra-high-performance fiber-reinforced concrete (UHPFRC), a special class of ultra-high-performance concrete (UHPC) incorporating a high dosage of discrete steel fibers, is characterized by considerable energy absorption due to its ultra-ductility, along with high tensile and compressive strengths, and is recognized as a promising material for resisting impact and blast loads in structures.

On the material side, extensive scientific research has been devoted to the compositions, microstructure, and mechanical properties of UHPC and UHPFRC. Comprehensive reviews by Du et al. [11] and Bajaber and Hakeem [12] summarized the progress in mixture design, hydration and microstructure development, and the resulting mechanical and durability performance, highlighting the role of optimized particle packing, low water-to-binder ratios, and high-volume supplementary cementitious materials. The effects of fiber type, geometry, and dosage on the mechanical properties of UHPC were systematically reviewed by Yang et al. [13], confirming that steel fibers govern the strain-hardening and multiple-cracking behavior that underpins the superior energy absorption of UHPFRC. These fundamental studies collectively established the material basis for the structural use of UHPFRC.

On the application side, UHPC and UHPFRC have been increasingly employed in practical engineering. Xue et al. [14] reviewed the rapidly growing application of UHPC in bridge engineering, including girders, deck panels, and connections, while the use of UHPC and UHPFRC for strengthening and retrofitting existing RC structures has been critically reviewed by Zhu et al. [15] and Huang et al. [16], respectively. These applied studies demonstrate that the superior strength, ductility, and durability of the material can be translated into structural-level benefits; they also reveal that impact and accidental loading remain among the most demanding, yet least standardized, design scenarios for such structures.

Several studies have demonstrated UHPFRC's enhanced impact resistance, primarily attributed to its excellent performance in resisting crack development and propagation [17,18]. While extensive research has focused on UHPFRC panels' resistance under medium/high-velocity impacts (20–500 m/s), such as those from tornado debris, aircraft accidents, and blasts [19–23], there is a scarcity of studies on UHPFRC's resilience and damage evaluation under low-velocity impacts below 10 m/s, typical in incidents such as falling objects, vehicle, and vessels collisions.

Existing low-velocity impact tests on UHPFRC exhibit a wide range of test conditions and member sizes. Ranade et al. [3] conducted repeated drop-weight tests on simply supported UHPFRC slabs using a 16 kg impactor and two cylindrical heads of different diameters (50 mm vs. 75 mm). The slabs were observed to progressively lose their resistance with increasing number of impacts, and the failure mode shifted from flexural failure to punching shear when the smaller impactor head was used. Additionally, the peak contact force decreased more rapidly under multiple impacts at higher velocities. Othman and Marzouk [7] investigated and compared the impact performance of 100 mm thick simply supported square plates made from reinforced high-strength concrete (HSC) and UHPFRC, using a 475 kg mass dropped repeatedly at a velocity of 10 m/s. The test results showed that the UHPFRC specimens failed in flexure and exhibited superior damage resistance compared to the HSC specimens. Farnam et al. [24] conducted drop-weight tests on 23 mm thick high-performance fiber reinforced concrete (HPFRC) plates, clamped on all four sides, using an 8.5 kg cylindrical impactor at a velocity of 4.23 m/s. On average, the plates were able to withstand five impacts before failing due to perforation. Zaini [25] conducted impact tests on 25 mm thick undamaged and pre-damaged UHPFRC plates under fixed boundary conditions. According to the test results, the maximum resistance of the pre-damaged plates was approximately 50–85% of that of the undamaged plates. Khan et al. [26] demonstrated the benefit of increasing the steel fiber content (2%, 4%, 6%) in 750 × 750 × 50 mm clamped slabs subjected to repeated drops of a 21 kg impactor. At a representative energy level of 1566 J (eighth drop), the 2% fiber mix exhibited severe damage and a central deflection of 8.95 mm, whereas higher fiber dosages reduced deflections and enhanced energy absorption. Jia et al. [27] tested reinforced UHPC members under low-velocity lateral impacts and showed that, in contrast to RC counterparts failing in shear, UHPC members sustained only minor flexural damage; a continuous surface cap model was further developed to reproduce the tests. Taken together, these studies consistently demonstrate cumulative deterioration under repeated impacts. Ranade et al. [3] identified a flexural-to-punching transition with a progressive decrease in peak contact force. Wei et al. [9] attributed the progressive stiffness loss to the degradation of fiber bridging, and Khan et al. [26] quantified the effect of fiber dosage on deflection growth and energy absorption. However, in these studies, the specimens were mostly simply supported beams or slabs, the degradation of stiffness was inferred indirectly (e.g., from peak contact force or deflection growth) rather than measured in a full-field manner, and the accompanying numerical simulations, where performed, addressed single-impact events only. A sequential modelling strategy capable of transferring accumulated damage fields across successive impacts, calibrated by independent material tests and evaluated against full-field measurements under fully fixed boundaries, has not yet been reported.

Investigations into the impact behavior of RC plates have revealed that the support configuration significantly influences energy absorption capacity, damage type, crack pattern, and acceleration response [28]. However, only a limited number of studies have examined such effects on UHPFRC plates, highlighting the need for further research. This gap is partly due to the experimental difficulty of realizing and verifying truly fully fixed boundaries under impact, which requires high-stiffness fixtures, management of severe edge stress concentrations, and complex instrumentation—challenges exacerbated by a lack of standardization.

Finite element (FE) analysis is a powerful tool to generalize and interpret experimental observations, as well as to probe parameter sensitivities not readily tractable in the laboratory [29]. Complementary to numerical approaches, analytical frameworks have

https://doi.org/10.3390/buildings16163300

also been developed to efficiently predict the dynamic response of structures under impulsive loading [30], offering valuable theoretical context for interpreting impact-induced response characteristics. However, most FE simulations of UHPFRC impact response have predominantly focused on single-drop events [3,31–33], leaving a gap in accurately modelling repeated impact loading and the associated mechanisms of progressive damage accumulation in UHPFRC plates. The development of such models is intrinsically dependent on high-quality experimental data for validation. Traditional discrete sensors are often inadequate for capturing the full-field, transient response during impact, whereas high-speed 3D digital image correlation (3D DIC) provides rich, full-field kinematic data indispensable for understanding complex failure mechanisms and delivering stringent benchmarks for model validation [34,35].

As a contribution toward addressing the aforementioned research gaps, this study presents an integrated experimental and numerical investigation into the low-velocity repeated impact response of a 50 mm thick UHPFRC plate with nominally fixed boundaries. The present work addresses two interrelated problems: a scientific problem, namely how damage initiates and accumulates in a nominally fixed UHPFRC plate under successive low-velocity impacts, and how this cumulative degradation governs the transition from flexural to punching shear failure. The second is an applied engineering problem, namely how the residual condition and remaining capacity of such protective components can be quantified from measurable impact responses to support damage assessment in practice. The primary objectives are to (i) experimentally characterize the progressive damage evolution, energy dissipation, and failure mechanisms of a fixed UHPFRC plate under repeated low-velocity drop-weight impacts; (ii) employ high-speed 3D DIC to capture high-resolution quarter-field transient kinematics, reconstructed to the full field by the verified test symmetry, thereby quantifying global and local structural responses during the transient impact events; and (iii) develop and evaluate a FE model that accurately predicts the dynamic response and cumulative damage, using the DIC data and observed damage patterns as a benchmark. Through this integrated approach, the study aims to provide novel insights into the behavior of fixed UHPFRC plates, deliver a predictive tool, and ultimately contribute to the resilient design of protective structural components.

2. Experimental Program

The experimental program was organized in six sequential steps: material preparation and mix design (Section 2.1), plate casting and curing (Section 2.2), mechanical characterization (Section 2.3), assembly of the nominally fixed test configuration (Section 2.4), instrumentation and data acquisition (Section 2.5), and the repeated impact schedule with the associated data processing (Section 2.6). The drop height, i.e., the impact energy per drop, served as the single variable factor of the impact program, while the sampling rate was optimized separately (Section 2.6). The measured output indicators comprised crack patterns, acceleration–time, strain–time, and displacement–time histories, and the impactor rebound velocity.

2.1. Materials and Mix Proportion

The materials and mix proportions of the UHPFRC developed for this study are shown in Table 1. The geometrical and mechanical properties of the straight micro-steel fibers (Bekaert, Zwevegem, Belgium) used are shown in Table 2. The particle size distribution of silica sand (Norman Emerson Group, Craigavon, Co., Armagh, UK), cement (CEM I 52.5N, Quinn Cement, Derrylin, UK) and ground granulated blast-furnace slag (GGBS, Ecocem Ireland Ltd., Dublin, Ireland) are shown in Figure 1.

Table 1. UHPFRC mix proportion (kg/m³).

Silica Sand	CEM I 52.5N	GGBS	Microsilica Slurry (MSS)	Water	SP	Steel Fiber (2% by Volume)
999.4	627.3	399.2	203.7	94.6	32.8	156.8

Table 2. Properties of steel fibers.

Diameter, d_f (mm)	Length, l_f (mm)	l_f/d_f	Density (g/cm³)	Tensile Strength, f_t (MPa)	Elastic Modulus, E_f (GPa)
0.2	13	65	7.84	2000	200

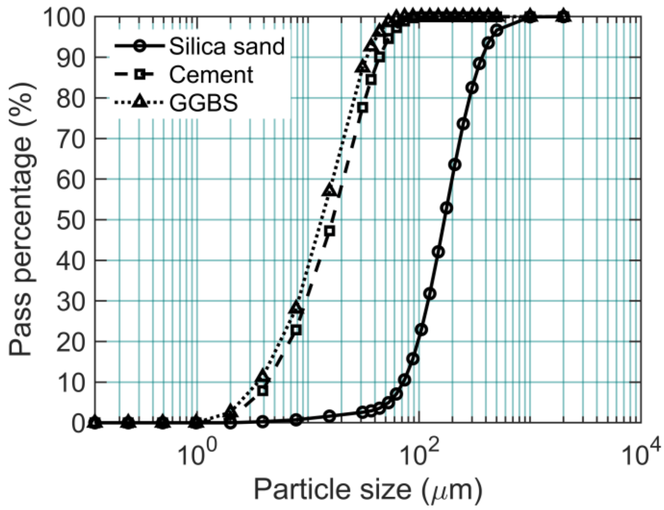

Figure 1. Particle size distribution.

The mixing procedure began with dry mixing the cement, GGBS, and silica sand for 2 min. The microsilica slurry (MSS, Elkem Microsilica®, Elkem ASA, Oslo, Norway) was then gradually added, followed by the premixed water and superplasticizer (SP, Sika® ViscoCrete® Premier, Sika AG, Baar, Switzerland). This mixture was blended for 15–20 min until a flowable consistency was achieved. Finally, the steel fibers were added and mixed until uniformly dispersed. The resulting fresh mix exhibited a slump flow of 750 mm, indicating good workability.

Following casting, all specimens were covered with a plastic sheet and cured under ambient conditions for 24 h. They were subsequently demolded and subjected to post-set curing in 90 °C water for 27 days, before being stored at ambient laboratory conditions until the day of testing.

2.2. Size and Details of UHPFRC Plate

The UHPFRC plate specimens had dimensions of 700 × 700 × 50 mm. It featured six holes, each with a diameter of 22 mm, spaced 120 mm apart on each side, as shown in Figure 2. These holes were specifically designed to facilitate the attachment of the plate to the supporting rig, thereby allowing the four sides of the plate to be considered fixed. During the casting process (Figure 3), the self-levelling UHPFRC was poured into the center of the mold and allowed to flow radially outwards. This casting method is known to induce a preferential fiber alignment perpendicular to the radial flow direction [36]. The molds were filled to capacity and the surface was troweled flat.

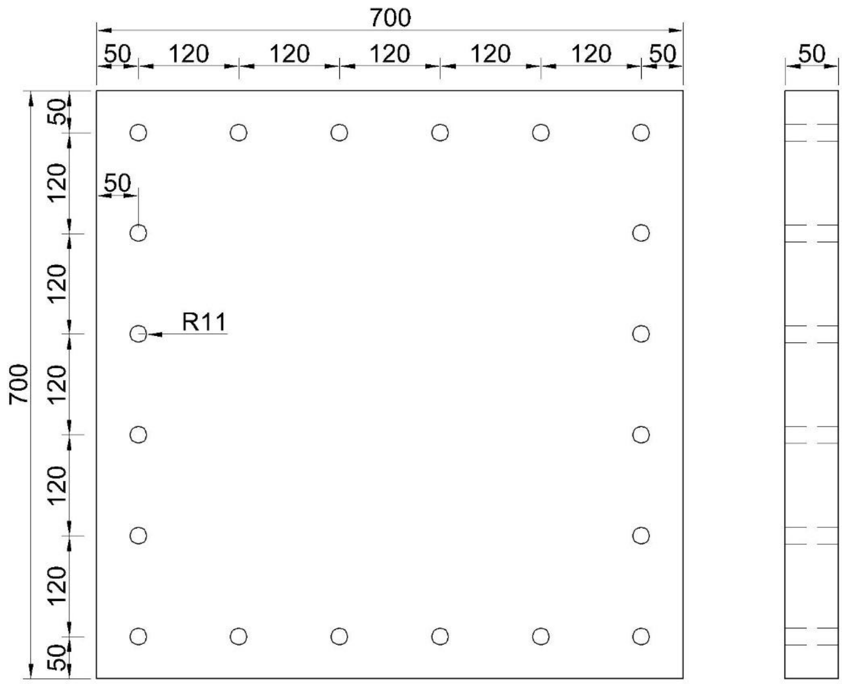

Figure 2. Geometry of the UHPFRC plate (unit: mm).

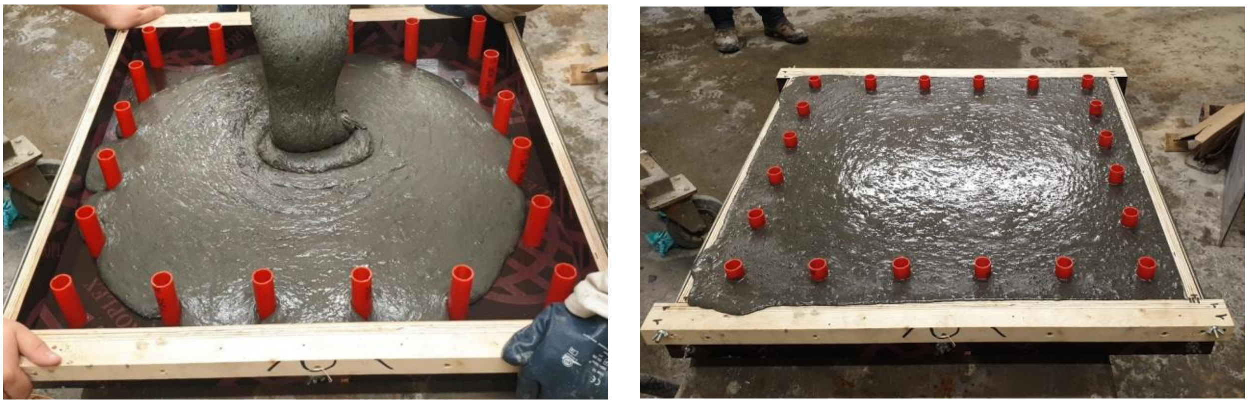

(**a**) (**b**)

Figure 3. Casting of the UHPFRC plate: (**a**) during casting; (**b**) after casting.

2.3. Mechanical Tests

Uniaxial compression tests following ASTM C39/C39M [37] were conducted on three cylindrical specimens with a diameter of 60 mm and a length of 120 mm. The cylinders were cast and cured identically to the plate specimens. A 3000 kN capacity universal testing machine applied the load at a displacement rate of 0.3 mm/min to capture both pre- and post-peak behavior. Two rigid rings were positioned at two-thirds of the specimen's height to define the gauge length. Axial deformation was measured using four LVDTs placed at 90° intervals (see Figure 4) to calculate compressive strain during the elastic stage. After cracking occurred, these LVDTs became unreliable due to crack propagation and rotation of the clamp screws; therefore, crosshead displacement was used to capture the nonlinear behavior in the later stage. The complete stress–strain curve was constructed by combining LVDT data from the elastic stage with crosshead displacement data from the post-cracking stage. The mean compressive strength f_{cm} was 176 MPa, with a standard deviation of 1.9 MPa (coefficient of variation 1.1%, n = 3). The static elastic modulus was determined from the ascending branch of the compressive stress–strain curves, giving $E_c = 50$ GPa (standard deviation 3.4 GPa, n = 3).

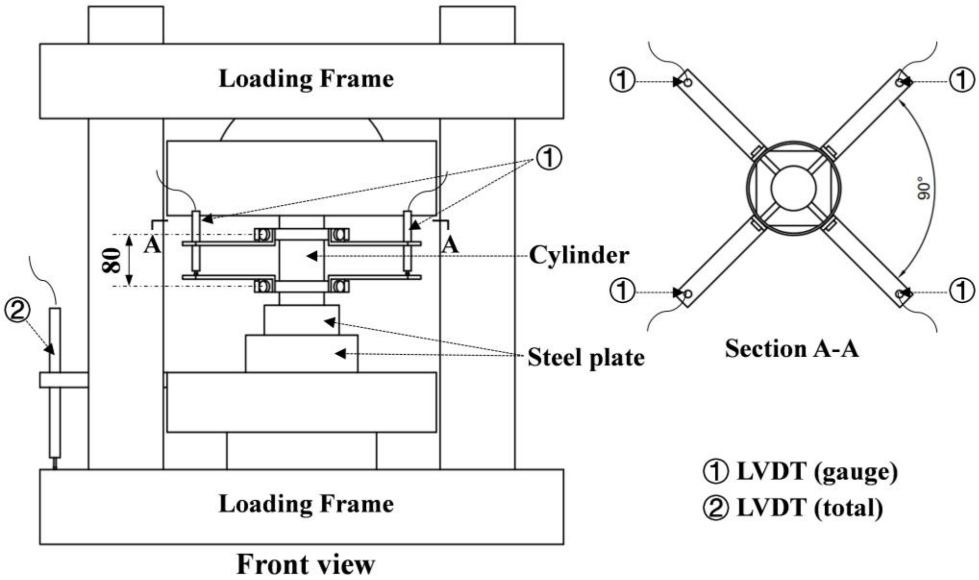

Figure 4. Compression test setup (all dimensions in mm).

The tensile behavior of UHPFRC was obtained using inverse analysis (IA). This method involves iteratively adjusting a pre-defined tensile law in a numerical model until its simulated response matches experimental data. The required experimental data were obtained from three-point bending (TPB) tests on four notched prisms, as shown in Figure 5. The tests were performed under crack-mouth opening displacement (CMOD) control, with loading rates of 0.05 mm/min up to 0.1 mm CMOD and 0.2 mm/min thereafter. As shown in Figure 6, the load-deflection curve predicted by the calibrated IA model exhibits good agreement with the experimental TPB results, confirming the reliability of the identified tensile parameters. The final constitutive models for compression and tension are presented in Section 4.2.

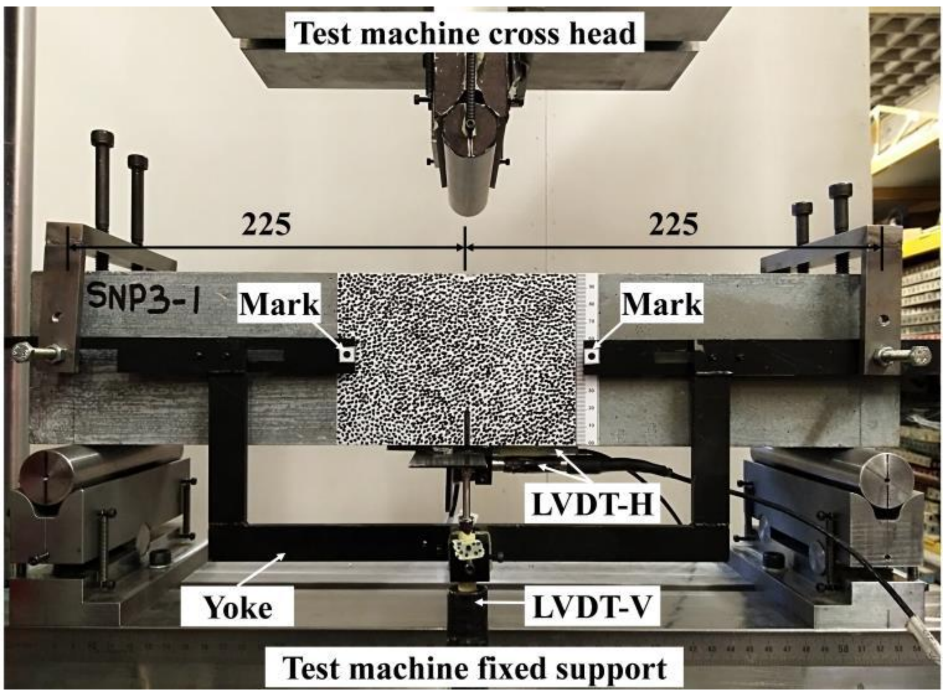

Figure 5. Three-point bending test setup.

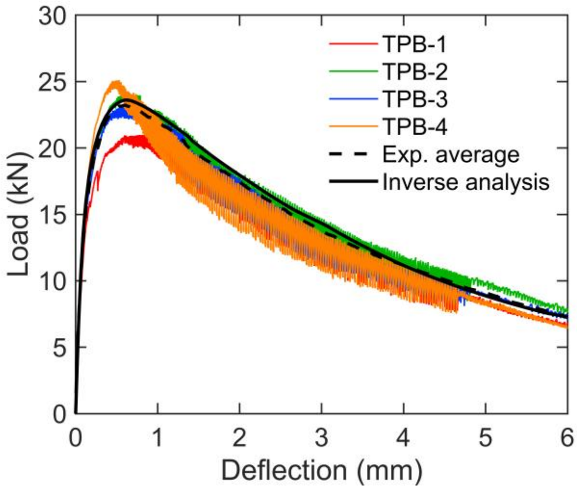

Figure 6. Experiments and inverse analysis for TPB test of beam.

2.4. Drop-Weight Test Setup

Repeated impact tests were performed using a custom-built drop-weight apparatus, as shown in Figure 7. The setup consists of a 40 kg bullet-shaped impactor with a 100 mm diameter hemispherical head, guided by two 6 m tall steel channels (125 × 115 mm). An electromagnet was used to lift and release the impactor from pre-determined heights.

The UHPFRC plate was mounted onto a rigid steel supporting rig (Figure 8). This supporting rig, designed to minimize energy absorption and ensure reliable test data [38], was constructed from welded rectangular hollow sections and bolted to a 30 mm thick base plate. A 50 mm thick steel clamping ring (700 × 700 mm outer, 500 × 500 mm inner dimensions) was used to secure the specimen with twenty M20 bolts, each tightened to a torque of 110 N·m [25], thereby realizing a nominally fixed boundary condition.

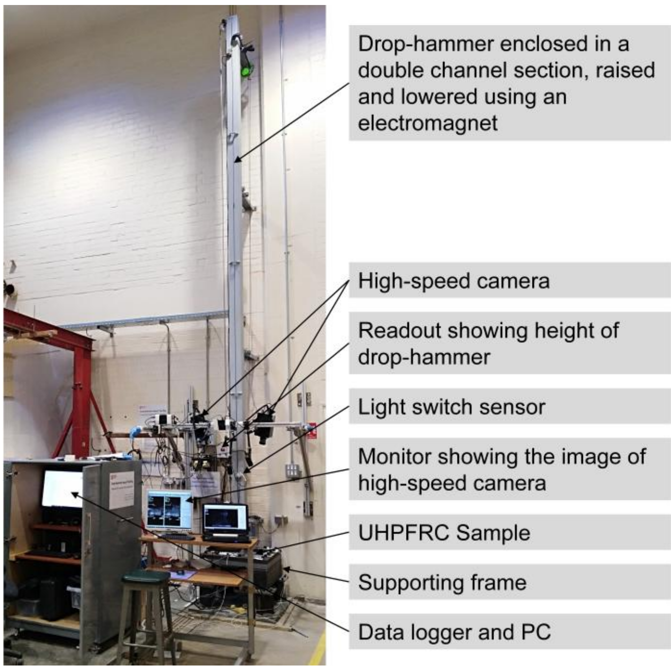

Figure 7. Drop-weight test rig.

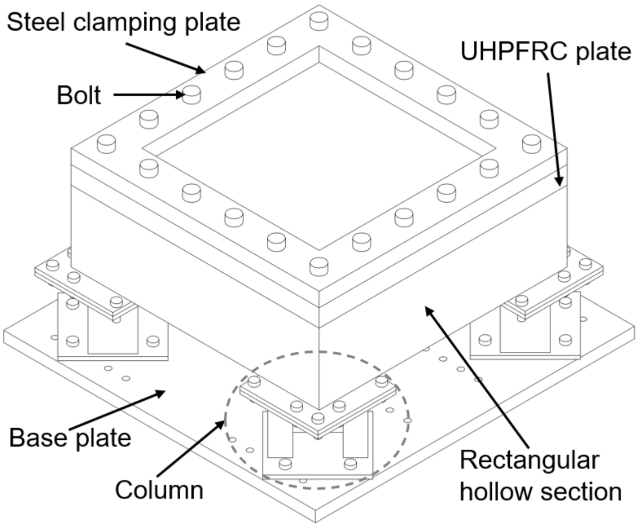

Figure 8. Schematic of the supporting rig.

2.5. Instrumentation and Data Acquisition

The instrumentation and data acquisition (DAQ) system is shown in Figure 9. As shown in Figure 10, the plate was instrumented with accelerometers (±10,000 g) and strain gauges. All sensor data were recorded using a Keysight U2356A DAQ system (Keysight Technologies, Santa Rosa, CA, USA) with a maximum aggregate throughput of 500 kSa/s, which was shared among the active channels. The impactor acceleration was not measured since mounting a data cable on the impactor would expose it to severe damage risks during the test.

To capture the transient kinematics of the plate over a quarter-field, a high-speed 3D digital image correlation (DIC) system was employed. The system comprised a pair of Photron FASTCAM SA4 cameras (Photron USA, Inc., San Diego, CA, USA) in a stereo configuration, triggered by an optical switch. Flicker-free LED (Correlated Solutions, Inc., Irmo, SC, USA) lighting provided stable illumination [39]. The surface of the plate facing the cameras was prepared with a random speckle pattern consisting of a white base coat and 3–5 mm black dots.

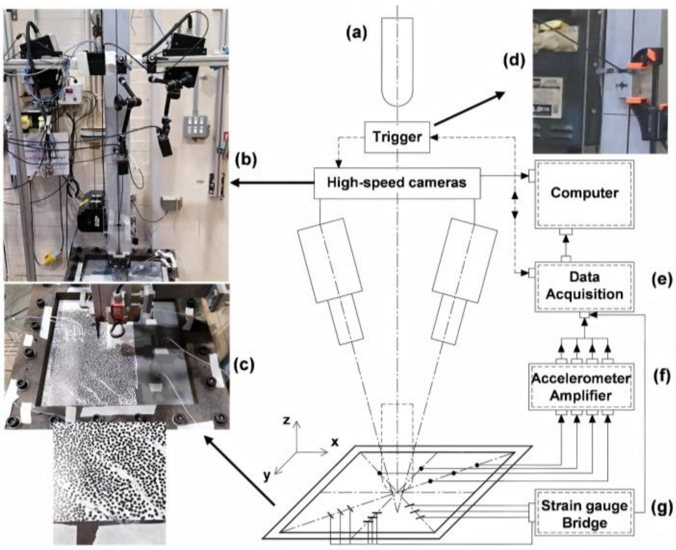

Figure 9. Experimental setup and data acquisition: (**a**) impactor; (**b**) two high-speed stereo vision cameras; (**c**) test plate with pattern; (**d**) trigger clamped on the channel; (**e**) data acquisition (U2356A

USB Analog Module); (**f**) power supply/signal conditioner for accelerometers; (**g**) customized bridge module for strain gauges.

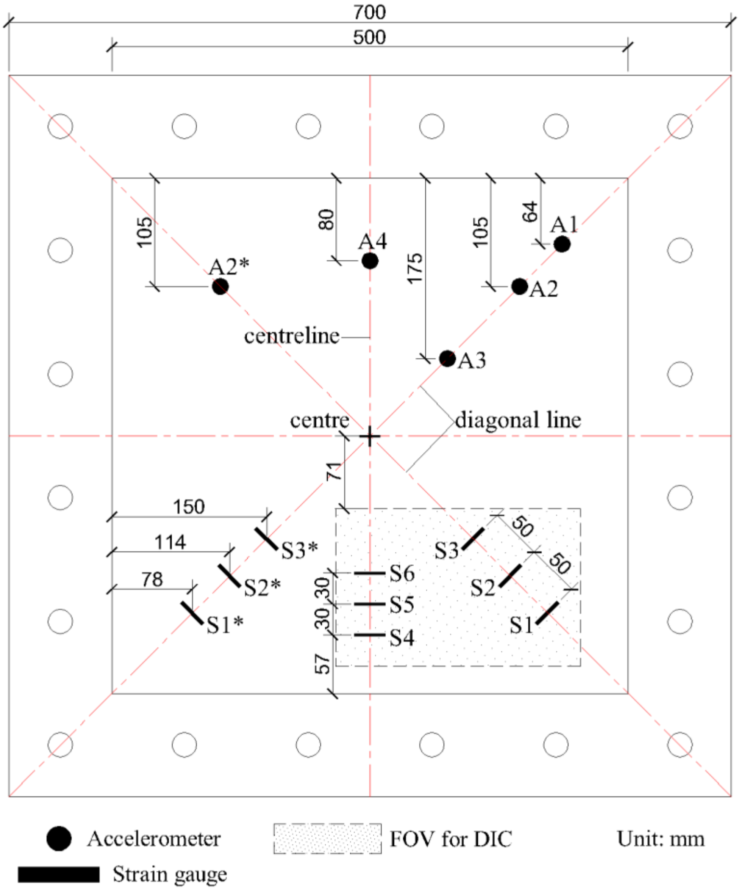

Figure 10. Arrangement of accelerometers, strain gauges, and field of view (FOV) for DIC. Labels marked with an asterisk (*) denote the counterpart sensors placed at the symmetric positions used to verify the test symmetry.

2.6. Test Schedule and Data Processing

The repeated impact test schedule is presented in Table 3. A 40 kg impactor was first dropped eight times from a height of 0.5 m. Subsequently, the drop height was increased to 2.0 m and then to 3.0 m for further impacts to induce progressive damage. Accurate acceleration histories can be obtained by recording as much data as possible during impact events, which requires using the highest feasible sampling rate [40]. Because the total throughput of the DAQ is fixed, a higher per-channel sampling rate can only be obtained by reducing the number of simultaneously active channels. A dedicated sampling rate study was therefore carried out during the first through eighth drops, for which the drop height was kept constant at 0.5 m.

Table 3. Test schedule.

Drop No.	Drop Height (m)	Energy (J)	Measurements					
			Data Acquisition			Digital Image Correlation		
			Sampling Rate Fs (kHz)	Acceleration	Strain	Frame Rate (kfps)	Displacement	Strain
1	0.5	196	5	/	S1–S6, S1*–S3*	10	A2, A3, A4	S1, S2, S4, S5, S6
2	0.5		10	/	S1–S6, S1*–S3*	10		
3	0.5		20	A2, A2*, A4	S1–S6, S1*–S3*	10		
4	0.5		35	A2, A2*, A4	S1–S6, S1*–S3*	10		
5	0.5		60	A2, A2*, A4	S1, S2, S4, S5	10		
6	0.5		120	A2, A4	S5	10		
7	0.5		250	A2, A4	/	10		
8†	0.5		25	A1, A2, A3	S1–S6, S1*–S3*	10		
9	2.0	784	25	A1, A2, A3	S1–S6, S1*–S3*	10		
10	3.0	1177	25	A1, A2, A3	S1, S2, S4, S5	10		

† During the eighth drop, disruption of the cameras resulted in the loss of the DIC record for this drop; the DIC data of the seventh drop at the locations away from the impact center (including A2) remained valid. * Denote the counterpart sensors placed at the symmetric positions.

Of note, 3D-DIC analysis was performed using Vic-3D v7 software. The field of view (FOV) covered a quarter of the plate, leveraging symmetry. The stereo camera system was calibrated using a standard procedure involving approximately 30 image pairs of a calibration target with 14 mm dot spacing, captured at various orientations [35,41], with the calibration residuals verified to be within the software-recommended tolerance. The accelerometer signals were conditioned by the built-in analogue anti-aliasing filter of the charge amplifier and subsequently low-pass filtered offline with a zero-phase fourth-order Butterworth filter with a 4 kHz cut-off frequency. All quantitative peak value comparisons in Sections 3.2 and 4.3 are based on drops acquired at 25 kHz or above. The 5 and 10 kHz records of the first and second drops under-resolve the initial peak and are used only qualitatively (Section 3.2). The DIC displacement fields were differentiated twice with respect to time to obtain velocity and acceleration histories at the positions listed in Table 3. Extracted coordinates and displacements were used for plate deformation surface fitting.

For validation purposes, acceleration–time and strain–time histories at the positions listed in Table 3. were also obtained from DIC at locations corresponding to the physical accelerometers. This cross-validation between discrete sensors and high-speed DIC measurements provided a cross-validated dataset for characterizing the impact response and for the subsequent validation of the numerical model. The key instrument specifications are as follows: accelerometer range of ±10,000 g (16-bit digitization, corresponding to a resolution of approximately 0.3 g); strain measurement accuracy of approximately 1%; and 16-bit DAQ resolution. The DIC calibration residuals are 0.03–0.1 pixels, corresponding, at the image scale of approximately 0.45 mm/pixel, to a physical displacement uncertainty of approximately 0.01–0.05 mm (below 2% of the smallest measured peak displacement). These specifications identify the uncertainty sources and measurement resolutions of each measurement chain. A full propagation of these uncertainties into the derived indices is beyond the scope of the present study, and the indices presented are therefore used for the relative comparison across the drop sequence rather than as absolute values.

3. Experimental Results

3.1. Crack Patterns

The evolution of damage on the top and bottom surfaces of the UHPFRC plate after the eighth, ninth, and tenth drops is shown in Figure 11. After the first seven drops from a height of 0.5 m, no visible cracks or surface damage were detected, indicating that the induced tensile stresses remained below the matrix's cracking threshold. The onset of visible damage occurred after the eighth impact (from 0.5 m). This manifested as a minor compressive indentation at the point of impact and the initiation of fine flexural micro-cracks on the bottom face.

(**a**)

(**b**)

Figure 11. Plate damage after the eighth (0.5 m, left), ninth (2.0 m, middle), and tenth (3.0 m, right) drop: (**a**) top surface; (**b**) bottom surface.

The eighth drop produced a localized indentation at the impact point on the top surface and several micro-cracks on the underside. This indicates that although the impact energy from a single 0.5 m drop was insufficient to generate macroscopic damage, the cumulative effect of eight consecutive impacts led to progressive internal deterioration. This likely included local fiber-matrix debonding, micro-crack initiation along matrix weaknesses, and gradual stiffness degradation.

The ninth drop, performed from a height of 2.0 m, significantly altered the damage morphology. On the top surface, a well-defined damage zone developed around the impact site due to concentrated compressive stresses and near-surface crushing. On the bottom surface, prominent radial macro-cracks emanated from the central region, oriented along the principal tensile stress directions. Notably, these radial cracks ran approximately perpendicular to the preferential fiber alignment expected from the radial casting flow (Section 2.2), so that fiber bridging across the cracks remained effective. The formation of these cracks indicates that the plate's global response was dominated by flexural deformation, where tensile stresses at the tension face exceeded the matrix tensile strength, allowing cracks to propagate toward the supports.

The 10th drop, from a height of 3.0 m, imparted considerably higher kinetic energy, generating a semi-spherical indentation on the top surface with a diameter of approximately 65 mm and a depth of 13 mm. This indentation corresponds to localized compressive failure and partial material extrusion. Concurrently, the bottom surface exhibited both radial cracks and circumferential (ring) cracks surrounding the impact zone. The radial cracks were characteristic of flexural failure, while the circumferential cracks were indicative of a punching shear mechanism caused by through thickness stress wave concentration beneath the impactor. The combination of these features reflects a transition

https://doi.org/10.3390/buildings16163300

from predominantly flexural response to a mixed flexural–shear failure mode as the impact energy surpassed the plate's punching shear resistance.

3.2. Acceleration–Time History

The symmetry of the experimental setup was first confirmed by the near identical acceleration at corresponding symmetrical locations, i.e., accelerations at A2 and A2*, as shown in Figure 12, which justified the use of a quarter-plate DIC analysis to represent the entire specimen's behavior.

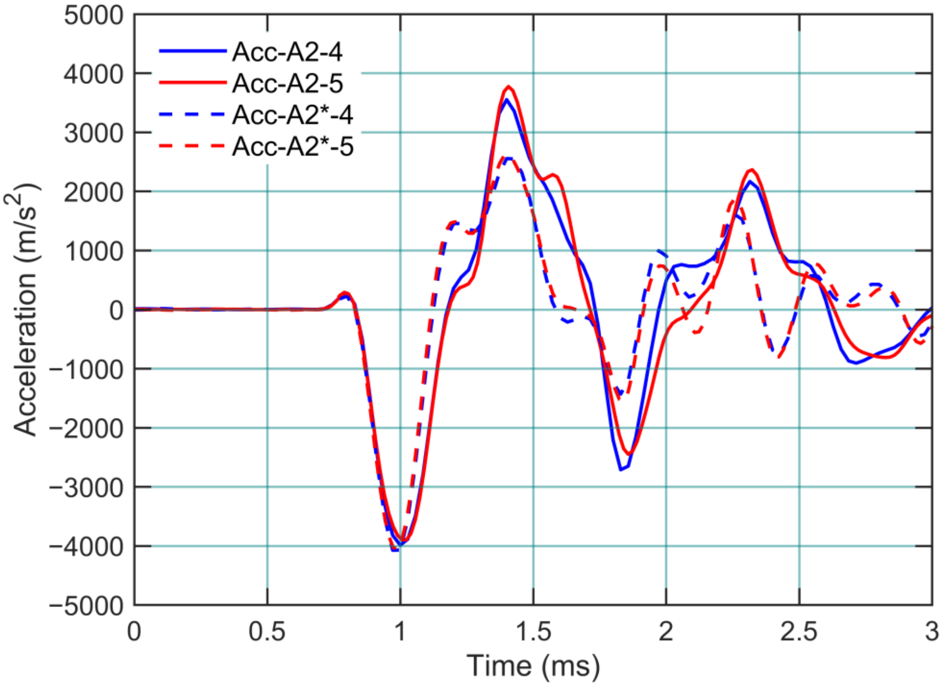

Figure 12. Accelerations measured at symmetrical positions.

The acceleration–time histories for the 0.5 m height drops, captured at positions A2 and A4 using accelerometers and DIC analysis, are presented in Figure 13 and Figure 14, respectively. A parametric investigation of the sampling rate showed that 25 kHz was optimal for capturing the transient response, as lower rates (e.g., 20 kHz) failed to resolve the signal adequately. A per-channel rate of 25 kHz was consequently adopted for the remaining drops since it resolved the transient peaks adequately while allowing all accelerometers and strain gauges to be recorded simultaneously. The 5 and 10 kHz rates used in the first and second drops were found to under-resolve the initial peak and the corresponding records are used only qualitatively. Furthermore, acceleration profiles derived from DIC displacement data were validated against physical accelerometer measurements. As shown in Figures 13 and 14, both methods yielded a strong correlation in peak values and overall patterns, confirming the reliability of the DIC-based measurements. A minor period extension observed in the DIC-derived curves is attributed to the numerical effect of the double differentiation process on the displacement data.

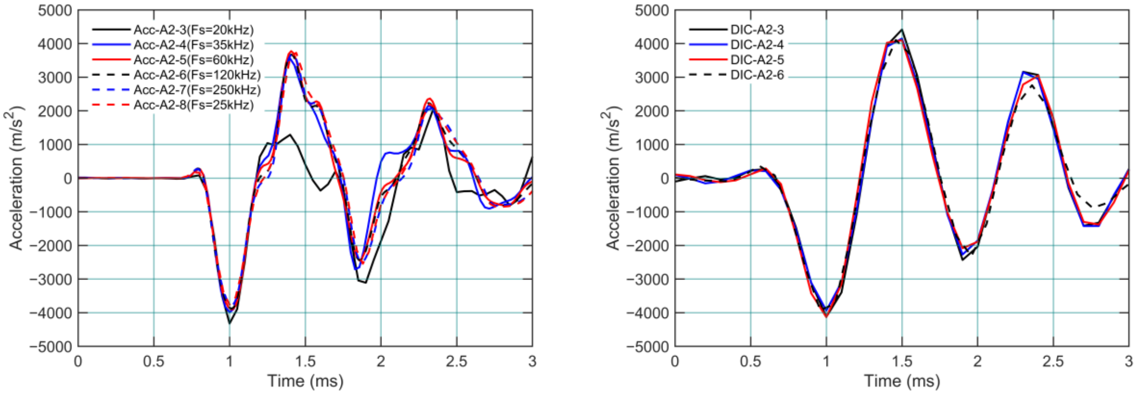

(**a**) (**b**)

Figure 13. Accelerations at A2 for the 0.5 m drop measured with (**a**) an accelerometer; (**b**) DIC.

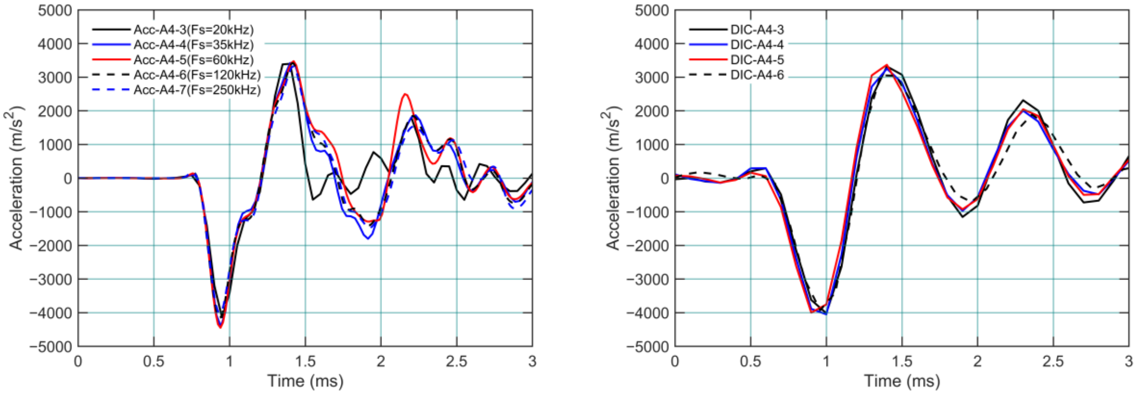

(**a**) (**b**)

Figure 14. Accelerations at A4 for drop height of 0.5 m measured with (**a**) an accelerometer; (**b**) DIC.

Figure 15 shows the acceleration–time histories for drops eight, ninth, and tenth measured by the accelerometers along the plate's diagonals. Analysis of the acceleration signals revealed the plate's damage progression. During the initial seven drops from 0.5 m, the acceleration–time histories were virtually identical, indicating a predominantly elastic response with negligible cumulative damage. This is consistent with the absence of visible cracking.

A critical shift in structural behavior was observed at higher impact energies (Figure 15). The increase in peak acceleration from the eighth (0.5 m) to the ninth (2.0 m) drop signifies that the plate was still structurally integral and capable of resisting the higher impact load through a global dynamic response. However, a decrease in peak acceleration was recorded during the tenth drop (3.0 m) compared to the ninth. This attenuation of the signal, despite higher impact energy, indicates a transition in the failure mode. The severe localized damage at the plate's center—characteristic of punching shear—absorbed a substantial amount of energy, which in turn inhibited the propagation of the dynamic response through the plate to the sensor locations.

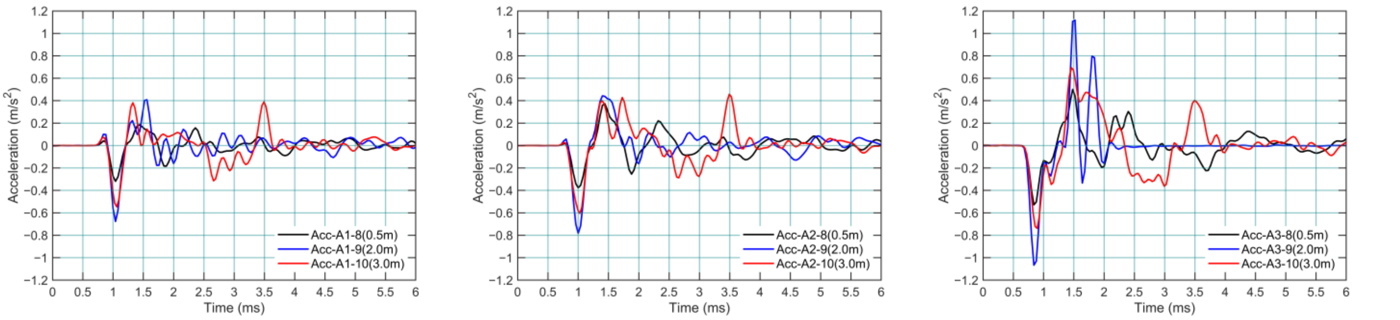

(**a**) (**b**) (**c**)

Figure 15. Accelerations from different drop heights for (**a**) A1; (**b**) A2; (**c**) A3.

3.3. Strain–Time History

Figure 16 shows the strain–time histories at symmetrical locations (S1–S3 vs. S1*–S3*). Strain measurements recorded at symmetrical locations exhibited close agreement across all drop heights, confirming the symmetry of the test setup and validating the applicability of quarter-plate DIC results to represent the full-plate behavior. Comparison between physical strain gauges and DIC-derived strains at varying drop heights (Figure 17) showed strong consistency in both magnitude and temporal evolution. On the top surface, the strain gauge area was subjected to compressive stresses immediately following impact, in line with the flexural response of the plate [42]. For the 0.5 m drops, results were highly repeatable, with minimal variation across successive impacts; thus, only the fourth drop is presented as a representative case. This agreement between DIC and physical gauge data across multiple impact energies substantiates the reliability of the DIC method for capturing transient strain fields under repeated impact loading. The absence of measurable divergence between data sources also indicates negligible structural degradation prior to the onset of visible cracking.

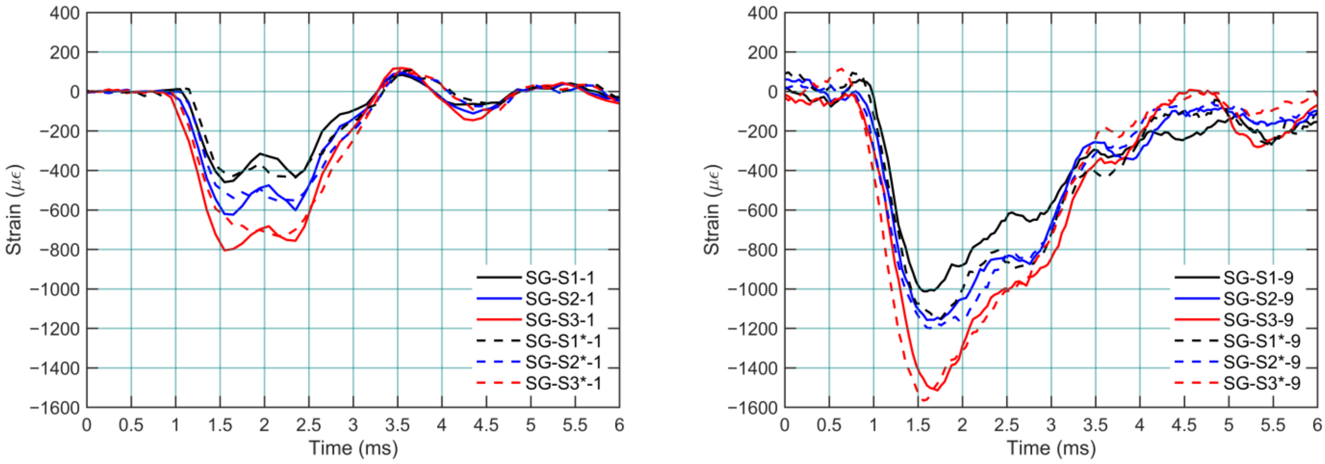

(**a**) (**b**)

Figure 16. Strains measured at symmetrical positions of (**a**) first drop; (**b**) ninth drop.

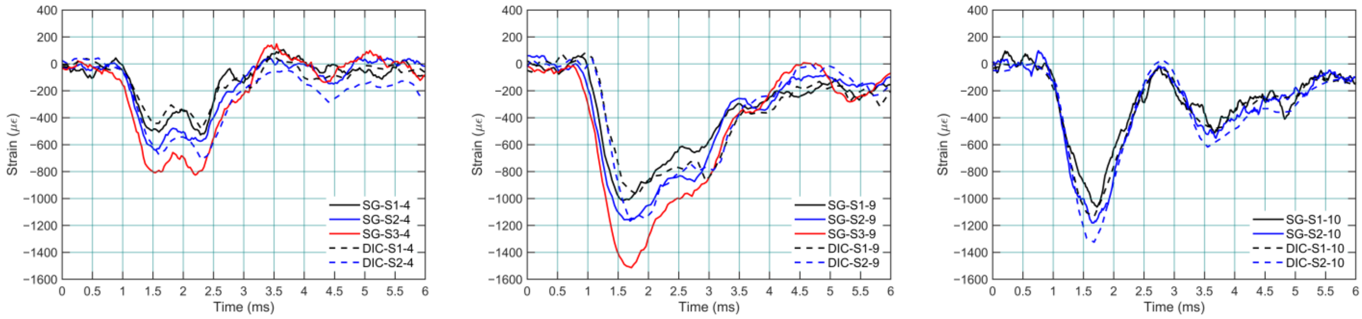

(**a**) (**b**) (**c**)

Figure 17. Strains measured from foil gauges (solid lines) and DIC (dashed lines) for (**a**) fourth drop; (**b**) ninth drop; (**c**) tenth drop.

3.4. Displacement–Time History

The displacement–time history, particularly the central deflection, is a primary indicator of a plate's global response and residual resistance following an impact event. Hereafter, the directly observed DIC region is termed the measured quarter field, and the symmetry-extended data the reconstructed full field. While direct measurement of the central point was precluded by the impactor's shadow, a symmetry-based reconstruction methodology was employed to determine the full-field kinematics. This approach involved capturing the displacement of a quarter-plate using DIC (Figure 18), exploiting the confirmed test symmetry to mirror the data into a global field (Figure 19), and then applying a polynomial surface fitting algorithm in MATLAB R2022a (The MathWorks, Inc., Natick, MA, USA) to interpolate the complete deflected surface for each time frame (Figure 20). Prior to the fitting, rigid body translation and rotation were removed from the DIC displacement data by referencing the measured field to the stationary clamped boundary region of the plate; the influence of residual support vibration was excluded by evaluating the permanent displacement only after the post-impact vibration had decayed. The adjusted R-squared values of the surface fits consistently exceeded 0.95 for every analyzed frame (Figure 21), indicating good agreement between the fitted surfaces and the measured data points, i.e., a small reconstruction error within the measured quarter. It is emphasized that the symmetry assumption underlying this reconstruction was verified experimentally at all energy levels through the symmetric sensor pairs (Sections 3.2 and 3.3), including the ninth drop at 2.0 m, for which the strains at symmetric locations remained in close agreement (Figure 16b). The possible suppression of asymmetric deformation in severely damaged states is acknowledged as a limitation in Section 5.3.

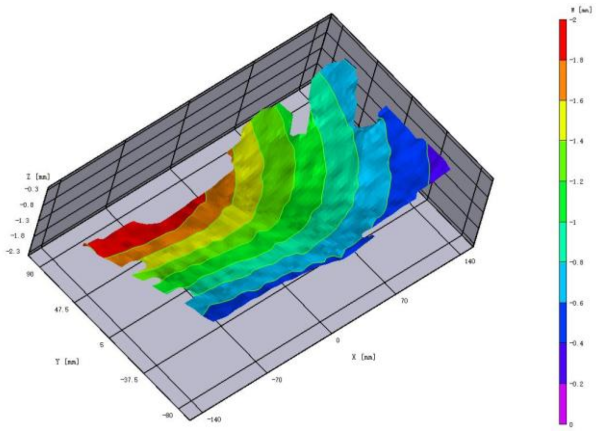

Figure 18. Displacement contour of one frame from DIC.

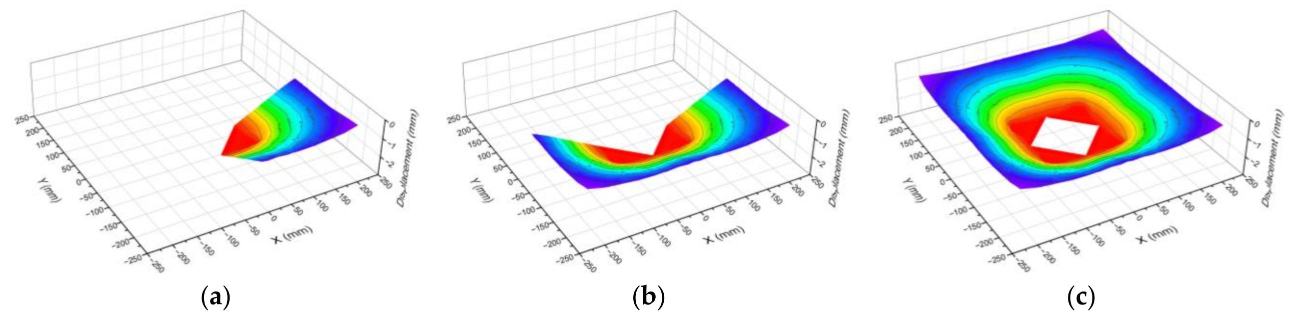

Figure 19. Displacement of the whole plate by taking advantage of the symmetry of the setup. (**a**) Symmetry to diagonal line; (**b**) symmetry to *Y*-axis; (**c**) symmetry to *X*-axis.

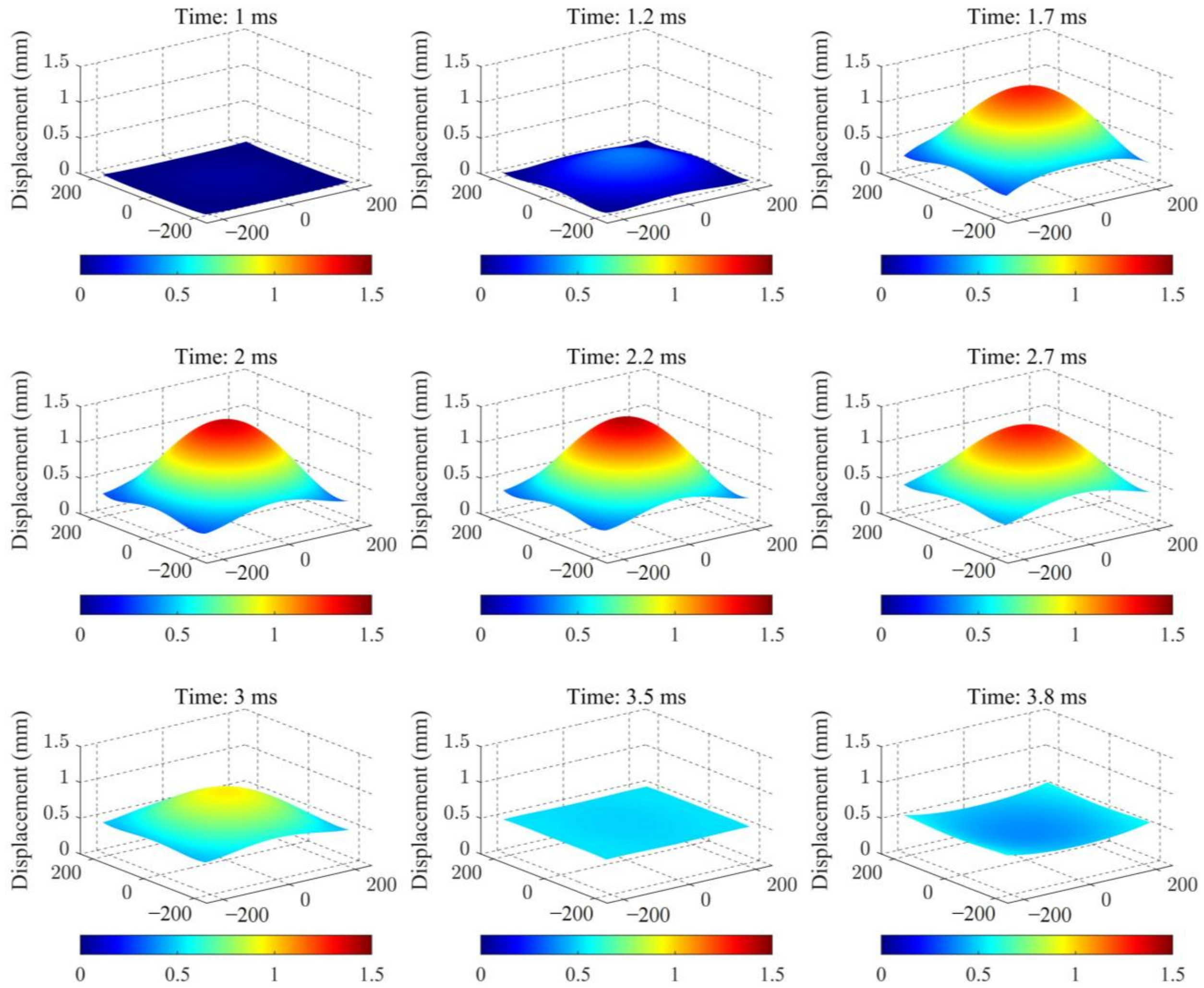

Figure 20. Full-field 3D displacement profile of plate in the initial part of the ninth drop.

Analysis of the reconstructed central deflection history reveals the progressive accumulation of damage. For the low-energy 0.5 m drops, the plate exhibited a classic elastic response, undergoing free vibration that returned to its original zero displacement equilibrium position. This behavior confirms that these initial impacts induced no significant plastic deformation or cumulative damage, which corroborates the findings from the acceleration–time history.

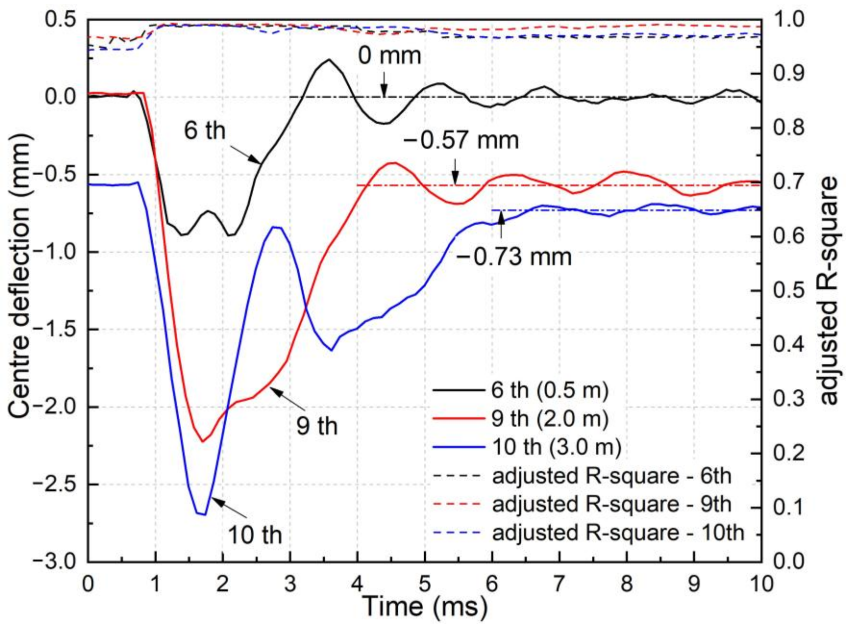

Figure 21. Deflection–time histories of center for repeated impact.

A marked transition in structural behavior occurred after the higher-energy impacts. Following the ninth drop from 2.0 m, the plate's post-impact vibration no longer returned to zero but instead shifted to a new equilibrium, resulting in a permanent displacement offset of 0.57 mm. This offset is a direct measure of the inelastic deformation and damage sustained by the plate. After the final 3.0 m drop, this permanent deformation increased to 0.73 mm, indicating further damage accumulation. It should be noted that modal indicators of stiffness degradation could not be extracted reliably from the present records because the free-vibration segment was truncated by the rebound and re-contact of the impactor; this is acknowledged as a limitation in Section 5.3.

3.5. Rebound Velocity

Direct instrumentation of the impactor was not feasible within the experimental setup. Therefore, the impactor's rebound velocity was estimated to characterize impactor reaction and to support the validation of FE model predictions against experimental data.

The impact velocity, $\mathrm{v_i}$, representing the velocity immediately prior to contact, was calculated from free fall theory:

$$v_i = \sqrt{2gh_0} \tag{1}$$

where h_0 is the drop height. This approach provided a consistent framework for linking experimental measurements to numerical predictions, while indirectly capturing the energy restitution characteristics of the impact events.

The rebound velocity was derived under the assumption that the rebound motion behaves as free fall. In this framework, the time required for the impactor to rise to its peak rebound height equals the time taken to fall back for a subsequent impact. This time interval, Δt, was measured as the duration between consecutive acceleration peaks in the plate's acceleration–time history (Figure 22). The rebound velocity, v_r, was then computed using the following:

$$v_r = \mathrm{g} \times \frac{\Delta t}{2} \tag{2}$$

where g is the gravitational acceleration, and Δt is obtained from accelerometer records at any plate location.

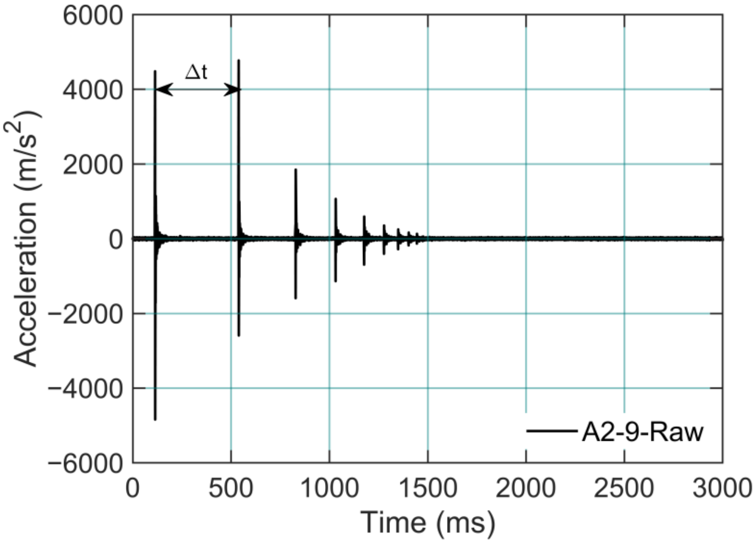

Figure 22. Example of acceleration signal.

3.6. Damage Evolution Indices

Based on the measured impact and rebound velocities, two damage evolution indices are further defined. The non-recovered impact energy of an impact (the energy not returned to the impactor), E_{abs}, is estimated as the difference between the incident kinetic energy and the rebound kinetic energy of the impactor:

$$E_{abs} = mgh_0 - ½mv_r^2 \tag{3}$$

where m is the impactor mass, and the small contribution of guide friction during the fall and rebound is neglected.

It should be emphasized that E_{abs} as defined in Equation (3) is the energy not returned to the impactor. It lumps together several contributions: the elastic vibration energy stored in the plate and subsequently dissipated by damping, the energy dissipated in the supporting frame, the bolts and the contact interface, the energy consumed by local crushing and friction at the contact surface, and the inelastic energy dissipated by cracking, fiber debonding, and fiber pull-out. E_{abs} is therefore used in this study as a relative indicator of the evolution of the restitution behaviour across the impact sequence and not as a direct measure of the energy dissipated by damage. Its interpretation as a damage indicator is supported here only when it is read together with the independent observations of crack pattern, residual displacement and peak resisting force. For terminological clarity, this quantity is referred to as the non-recovered impact energy throughout this paper, and the energy absorption ratio denotes its value normalized by the incident kinetic energy.

The energy absorption ratio, η, is then defined as follows:

$$\eta = E_{abs}/(mgh_0) \times 100\% \tag{4}$$

The model-assisted nominal secant stiffness, k_s, is defined as follows:

$$k_s = F_{pk}/\delta_{A2,max} \tag{5}$$

where F_{pk} is the force taken from the FE simulations, and is normalized by the value of the fourth drop. The DIC record of the eighth drop was lost owing to a disruption of the cameras during this drop. The indicator is termed nominal because it is defined from the peak force and the corresponding peak displacement rather than from a full unloading path and model assisted because the peak force is taken from the FE simulations; it is used for the relative comparison across the drop sequence. No stiffness values are reported for the first to third drops, which served to optimize the acquisition settings (Section 2.6).

These kinematics-derived indices, together with the residual central displacement δ_{res} obtained from the DIC-based reconstruction in Section 3.4, the peak displacement $\delta_{A2,max}$ measured by DIC at the accelerometer A2 location, and a model-assisted nominal secant stiffness indicator k_s, are summarised for each drop in Table 4.

Table 4. Impact energy, rebound velocity, energy absorption ratio, normalized model-assisted nominal secant stiffness indicator and residual displacement.

Drop No.	Drop Height (m)	v_i (m/s)	Δt (ms)	v_r (m/s)	Impact Energy, mgh_0 (J)	E_{abs} (J)	η (%)	$\delta_{A2,max}$ (mm)	F_{PK} (kN)	k_s (kN/mm)	Normalized k_s (-)	δ_{res} (mm)
4	0.5	3.13	425	2.08	196	109	56	2.56	119	46.5	1.000	0
5	0.5	3.13	418	2.05	196	112	57	2.57	118	45.9	0.988	0
6	0.5	3.13	423	2.07	196	110	56	2.61	118	45.2	0.973	0
7	0.5	3.13	421	2.07	196	110	56	2.63	116	44.1	0.949	0
8	0.5	3.13	422	2.07	196	110	56	-	115	-	-	-
9	2	6.26	443	2.17	784	690	88	5.83	134	23.0	0.494	0.57
10	3	7.67	207	1.02	1177	1155	98	5.15	113	21.9	0.472	0.73

$\delta_{A2,max}$: peak displacement measured by DIC at the accelerometer A2 location. Tabulated values are rounded for presentation; the energy absorption ratio and the normalized stiffness are computed from unrounded values (normalized by the unrounded fourth drop value) and may therefore differ in the last digit from the ratio of the rounded entries. Stiffness values are not available for the first to third drops (acquisition-optimization drops) or the eighth drop (DIC record lost).

The damage evolution indices in Table 4 quantify the progression of damage across the impact sequence. For the 0.5 m drops (fourth to eighth), Δt and the rebound velocity remained nearly constant, and correspondingly E_{abs} stayed essentially unchanged at approximately 110 J per drop, i.e., η = 56–57%, indicating a stable restitution response without apparent degradation under this moderate impact energy. Note that the first to third are not listed as the rebound velocity was not extracted for these drops, although their acceleration histories were virtually identical to those of drops fourth to eighth (Section 3.2). When the drop height increased to 2.0 m, the rebound velocity only marginally rose to 2.17 m/s despite the impact velocity doubling to 6.26 m/s; as a result, E_{abs} rose sharply to approximately 690 J (η = 88%), suggesting substantially enhanced energy dissipation through flexural cracking and plastic deformation. It should be noted that this measurement derives from a single test following eight prior impacts, so the increase may reflect both the high impact energy and cumulative damage. After the final 3.0 m drop, the rebound velocity dropped markedly to 1.02 m/s (an estimate to be treated with caution since the penetration that occurred violates the free-motion assumption most strongly for this drop), and η reached approximately 98%. This indicates that nearly the entire impact energy was consumed by local crushing and the punching shear failure rather than being returned to the impactor. This evolution of the energy-based indices is consistent with the crack patterns (Section 3.1), the attenuation of the peak acceleration (Section 3.2), and the increase in residual central displacement from zero to 0.57 mm and 0.73 mm (Section 3.4) and provides a quantitative description of the progressive degradation of the plate under cumulative impacts.

Two further measures of the stiffness degradation are included in Table 4. For the repeated 0.5 m drops, the loading conditions are nominally identical, so that the growth of $\delta_{A2,max}$ directly reflects the increase in compliance without requiring any force measurement—a force-independent, purely experimental indicator. Specifically, $\delta_{A2,max}$ rose by 2.6% from the fourth to the seventh drop, quantifying the cumulative damage under repeated sub-failure impacts. For the comparison across different energy levels, the model-assisted nominal secant stiffness indicator k_s combines the measured $\delta_{\mathrm{A2,max}}$ with the FE-predicted peak force (the reliance on model-derived forces is acknowledged in Section 5.3). The A2 location, offset from the impact center, ensures that the displacement represents the global flexural response, unaffected by the local indentation and punching penetration at the center and independent of the symmetry-based reconstruction under 0.5 m drops. Normalized by the fourth drop, k_s decreased gradually by 5.3% over the repeated 0.5 m drops, fell abruptly by 50.8% after the 2.0 m drop—marking the onset of the flexural-to-punching transition—and decreased by only a further 4.5% after the 3.0 m drop. This indicates that the global flexural stiffness had stabilized while the additional incident energy was consumed mainly by local penetration. Because the drop height and the prior damage state changed simultaneously at the ninth drop, the 50.8% reduction reflects the combined effects of the increased impact energy, the nonlinear structural response at the higher energy level, the accumulated damage, and the changing deformation mechanism, rather than damage accumulation alone. This evolution is consistent with the energy-based indices, the crack patterns (Section 3.1), and the residual displacements discussed above.

4. Numerical Simulations

4.1. Finite Element (FE) Model

Finite element (FE) simulations were performed to complement the experimental test and provide deeper insights into the dynamic response and damage evolution of UHPFRC plates under low-velocity impact loading. The simulations were conducted using ABAQUS 2020 (Dassault Systèmes Simulia Corp., Providence, RI, USA), with model parameters derived from the material tests (Section 2.3) or adopted from established practice (Section 4.2).

Exploiting the structural symmetry, a quarter model of the UHPFRC plate, the steel impactor, and components of the supporting rig were simulated (Figure 23). Plane symmetry constraints were applied on both the x–y and z–y planes. The base of the support structure was fully restrained in all degrees of freedom. Welded and bolted joints in the support frame were represented using tie constraints to ensure accurate load transfer. Contact between the UHPFRC plate and the clamping plate, and between the plate and the supporting rig, was modelled using hard contact for normal behavior and a penalty friction formulation with a friction coefficient of 0.2 for tangential slip resistance, using the default contact enforcement settings of ABAQUS/Explicit.

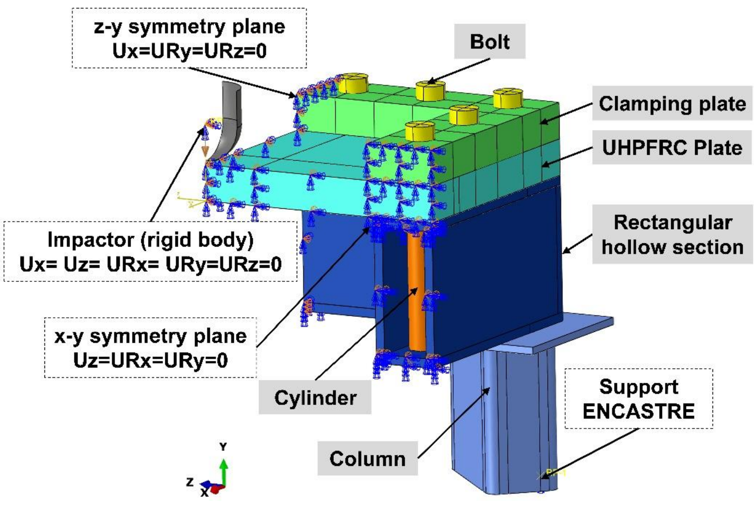

Figure 23. Geometry and boundary conditions of the FE model.

The steel impactor was modelled as a rigid body with a discrete mass positioned at its centroid, allowing only vertical translational motion. At the start of each simulation, the impactor was positioned 10 mm above the plate's surface and assigned an initial velocity (v_i) corresponding to the drop height (Table 4). The impact force was extracted as the resultant contact force between the impactor and the plate, which equals the product of the impactor mass and its simulated acceleration during contact.

The simulation was performed in two stages. The first stage, using ABAQUS/Standard, simulated the pretensioning of the bolts via the bolt load feature. At full pretension, the bolt length was fixed to maintain preload. The second stage, executed in ABAQUS/Explicit, captured the transient dynamic response to the impact load. The low-velocity impact was simulated using explicit time integration, with the deformed configuration and stress state obtained from the pretensioning step imported as the initial state of the impact analysis to reflect pre-load deformation effects. To realize the repeated impacts algorithmically, a sequential procedure was adopted. Here, the stress and damage fields at the end of each impact were imported as predefined initial conditions for the next drop via the Abaqus import capability, thereby preserving cumulative degradation across the impact sequence. The transferred state variables comprised the stresses, strains, plastic strains, and the damage variables (dt, dc); nodal velocities and accelerations were re-initialized to zero before each subsequent impact so that every drop started from the quasi-static deformed configuration inherited from the previous one.

The UHPFRC plate and steel components were discretized using 8-node reduced-integration brick elements (C3D8R). Mesh sensitivity studies were conducted with element sizes of 10 mm, 5 mm, and 2.5 mm, assessing convergence against peak contact force, maximum central deflection, and dissipated energy. A 5 mm element size achieved mesh-independent results for these metrics while maintaining computational efficiency and was therefore adopted. The energy balance was monitored in all explicit analyses. Following contact, the kinetic energy of the impactor was progressively converted into internal energy and dissipated through plasticity, damage, and contact friction; the ratio of the artificial strain (hourglass) energy to the internal energy remained below 5% at all times in every drop. The total energy also remained approximately constant after separation (drift below 0.1%), confirming the numerical stability of the simulations.

4.2. Material Models

The nonlinear behavior of UHPFRC was simulated using the concrete damaged plasticity (CDP) model available in ABAQUS. This model has been demonstrated to be effective in capturing the complex response of UHPFRC under both static [43] and impact loading conditions [31]. The CDP model combines isotropic damaged elasticity with isotropic tensile and compressive plasticity to represent the inelastic behavior. It is particularly well suited for this study as it allows for the definition of compression hardening, tension stiffening, progressive stiffness degradation (damage), and strain rate dependency. The CDP parameters adopted from established practice for UHPFRC under impact and punching shear simulations [31,44] are summarized in Table 5.

Table 5. Concrete damaged plasticity model parameters.

Parameter	Dilation Angle ψ (°)	Eccentricity	fb0/fc0	Kc	Viscosity Parameter
Value	36	0.1	1.16	0.67	0

The constitutive inputs were derived from the material tests in Section 2.3. The compressive stress–strain relationship comprises an ascending branch up to peak stress, followed by a descending softening branch (Figure 24a). The ascending branch was defined using the Sargin model [45] (Equation (6)), while the post-peak descending branch was modelled by a modified Carreira-type equation [46] (Equation (7)). Parameters include the mean compressive strength f_{cm}, modulus of elasticity E_c, secant modulus to peak E_{c1}, strain at peak compressive stress ε_{c1}, and ultimate compressive strain ε_{cu}. The shape parameters A (ascending) and B, C (descending) were obtained by fitting Equations (6) and (7) to the test data.

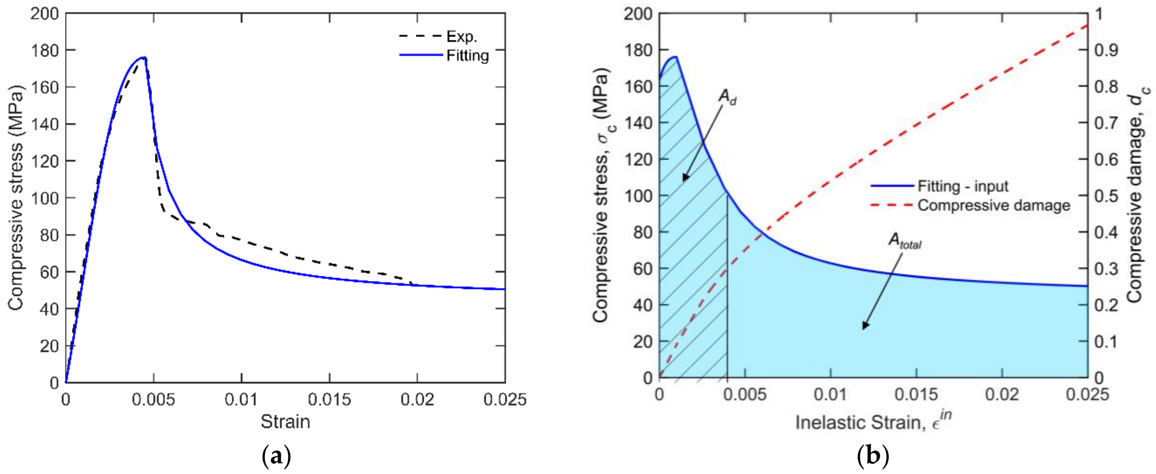

Figure 24. Compression input for UHPFRC: (**a**) compressive stress vs. strain; (**b**) compressive damage parameter vs. inelastic strain.

$$\text{ascending:} \, \sigma_c = f_{cm} \frac{\frac{E_c}{E_{c1}}\frac{\varepsilon_c}{\varepsilon_{c1}} + (A-1)\frac{\varepsilon_c}{\varepsilon_{c1}}^2}{1 + (\frac{E_c}{E_{c1}} - 2)\frac{\varepsilon_c}{\varepsilon_{c1}} + A\frac{\varepsilon_c}{\varepsilon_{c1}}^2}, \varepsilon_c < \varepsilon_{c1} \tag{6}$$

$$\text{descending:} \;\; \sigma_c = f_{cm} \frac{1}{B\varepsilon_c^C + 1 - B}, \varepsilon_{c1} < \varepsilon_c < \varepsilon_{cu} \tag{7}$$

The uniaxial tensile law was divided into three regimes (Equations (8)–(10)): linear elastic up to cracking strength f_{tck} at ε_{tck}; a strain-hardening branch up to the mean tensile strength f_{ctm} at ε_{tmax} (idealised as linear); and a softening branch defined as a function of crack opening displacement (COD) using an exponential fit to direct tension test data (Equation (10)).

$$\text{linear-elastic:} \;\; \sigma_t = E\varepsilon_t, \; \varepsilon_t < \varepsilon_{tck} \tag{8}$$

$$\text{strain-hardening:} \;\; \sigma_t = f_{tck} + \frac{f_{ctm} - f_{tck}}{\varepsilon_{tmax} - \varepsilon_{tck}}(\varepsilon_t - \varepsilon_{tck}), \varepsilon_{tck} < \varepsilon_t < \varepsilon_{tmax} \tag{9}$$

$$\text{softening:} \;\; \sigma_t = f_{ctm} e^{a\,w}, 0 < w < w_u \tag{10}$$

where w is the crack opening displacement, w_u is the maximum CMOD, and a is a fitting parameter determined from the inverse analysis (Section 2.3). The ultimate crack opening was taken as w_u = 6.5 mm, which corresponds to half the fiber length ($l_f/2$ = 6.5 mm) and is consistent with the assumption of complete fibre pull-out at the end of the softening branch.

The parameters, i.e., f_{tck}, f_{ctm}, ε_{tmax}, and a, were determined by matching FE and experimental load–displacement curves (Figure 6). The calibrated tensile stress–strain curve is shown alongside the experimental results in Figure 25.

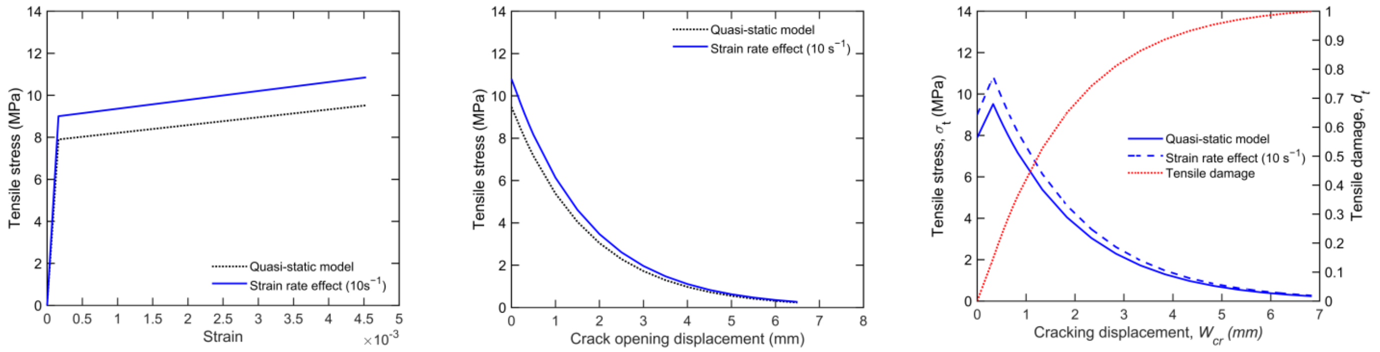

(**a**) (**b**) (**c**)

Figure 25. Tension input for UHPFRC: (**a**) tensile stress vs. strain (up to peak); (**b**) tensile stress vs. crack opening displacement (after peak); (**c**) tensile stress and damage parameter vs. crack opening displacement.

To ensure mesh objectivity in the post-peak tensile regime, the tensile softening law was converted from stress-strain to stress–displacement by multiplying strain by the characteristic element length [44] taken as $L_{cr} = \sqrt[3]{V}$, where V is the element volume.

The CDP tensile (*dt*) and compressive (*dc*) damage variables represent stiffness degradation due to inelastic deformation. In this study, compressive damage initiates beyond the limit of proportionality in compression, and tensile damage initiates at cracking strength. The damage evolution d was assumed proportional to the dissipated fracture energy relative to the total energy capacity, computed as the ratio of the area under the inelastic stress–strain (compression) or stress–COD (tension) curve to the total area under the corresponding envelope (Equation (11)). The resulting $dc(\varepsilon_{c,in})$ and dt(w) curves are shown as dotted lines in Figure 24b and Figure 25c, respectively.

$$d = \frac{A_d}{A_{total}} \tag{11}$$

for compression: $A_d = \int_0^{\varepsilon^{in}} \sigma_c d_\varepsilon$ and $A_{total} = \int_0^{\varepsilon_u^{in}} \sigma_c d_\varepsilon$ and for tension: $A_d = \int_0^{w^{cr}} \sigma_t d_w$ and $A_{total} = \int_0^{w_u^{cr}} \sigma_t d_w$.

Within the CDP framework, the effective stiffness is degraded as $(1-d)E_0$, so that the unloading and reloading moduli are governed directly by d. Defining d as the ratio of the dissipated inelastic energy to the total energy capacity therefore ties the stiffness degradation to the energy actually dissipated by inelastic micro-cracking, yielding a monotonic evolution bounded between 0 and 1.

UHPFRC exhibits rate sensitivity, particularly in tension. The effect is typically quantified by a dynamic increase factor (DIF). The literature indicates modest or negligible rate effects in compression below approximately 30 s^{-1}, but more pronounced increases in tensile strength with rate [46–48]. The experimental strain rates, obtained from the strain gauges and the DIC-derived strain fields, reached a maximum of approximately 4 s^{-1}, a ceiling of about 2.5 times the maximum measured rate was imposed to prevent extrapolation of the DIF beyond the range covered by the source data. At this level, the strength enhancement is modest, so the predicted response is insensitive to the exact value of the ceiling. Strain rate enhancement was applied only to the tensile response using the formulation by Thomas and Sorensen [48], as shown by the dashed line in Figure 25. No compressive DIF was applied within the present rate range.

For completeness, the full set of constitutive values used in the FE model is as follows: $E_c = 50$ GPa and $\upsilon = 0.2$; the compressive law of Equations (6)–(7) with $f_{cm} = 176$ MPa; the tensile law of Equations (8)–(10) with $f_{tck} = 7.9$ MPa, $f_{ctm} = 9.52$ MPa, $\varepsilon_{tck} =$

0.0158%, ε_{tmax} = 0.453%, $a = -0.57$ mm^{-1}, and w_u = 6.5 mm; the energy-based damage law of Equation (11); the tensile DIF with a ceiling of 10 s^{-1}; and the CDP parameters listed in Table 5.

The steel components of the rig were assumed to remain within their elastic range and were modelled as a linear elastic material with a density of 7800 kg/m^3, a Young's modulus of 210 GPa, and a Poisson's ratio of 0.3.

Damping was considered via two mechanisms available in ABAQUS/Explicit: bulk viscosity and Rayleigh (material) damping. Bulk viscosity (linear = 0.06; quadratic = 1.2, ABAQUS defaults) was used to suppress spurious high-frequency volumetric oscillations typical in impact simulations. Rayleigh damping defines the viscous damping matrix C as a linear combination of the mass (M) and stiffness (K) matrices:

$$C = \alpha_0 M + \beta_0 K \tag{12}$$

The mass and stiffness proportional coefficients (α_0, β_0) can be obtained from two target modes i and j with circular frequencies ω_i, ω_j and viscous damping ratios ξ_i, ξ_j [49]:

$$\alpha_0 = \frac{2\omega_i\omega_j(\xi_i\omega_j - \xi_j\omega_i)}{\omega_j^2 - \omega_i^2} \tag{13a}$$

$$\beta_0 = \frac{2(\xi_j\omega_j - \xi_i\omega_i)}{\omega_j^2 - \omega_i^2} \tag{13b}$$

In this study, α_0 and β_0 were initially estimated from the first two modes with a viscous damping ratio of 0.005. As shown in Figure 26, the inclusion of Rayleigh damping had a negligible effect on the primary response metrics (plate displacement and impactor acceleration) but increased the computational time threefold. Consequently, for computational efficiency, only the default bulk viscosity damping was employed in the final simulations.

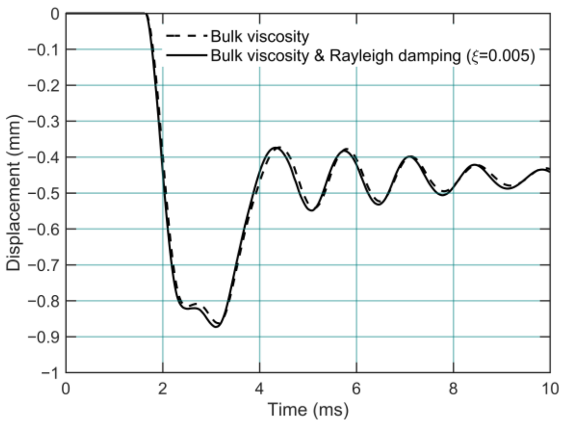

(**a**)

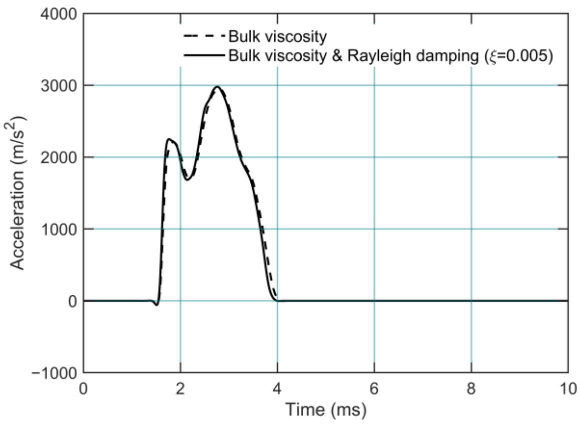

(**b**)

Figure 26. Effect of damping on the results of (**a**) displacement–time histories of plate; (**b**) acceleration–time histories of impactor.

4.3. Numerical Simulation Results

The predictive capability of the FE model was assessed by a direct comparison of its predictions against the measured responses from the drop-weight impact tests. Figures 27–31 present the comparison of the time history responses of strain (S2, S3), acceleration

(A3), displacement (A3), and rebound velocity, with the corresponding peak values summarized in Table 6. The numerical results showed good agreement with the experimental data in terms of both the time histories of responses and the peak values.

The model demonstrated predictive capability for strain (Figures 27 and 28) and displacement (Figure 29). Model-to-test ratios for peak strains at S2 and S3 ranged from 0.86 to 1.01, with smaller scatter than for displacement at A3 (0.92–1.30). Residual strains were also closer to experimental values than residual displacements. This likely reflects higher accuracy of foil strain gauges compared with DIC, which can be influenced by rig vibration and minor impactor tilt—both idealized in the FE model.

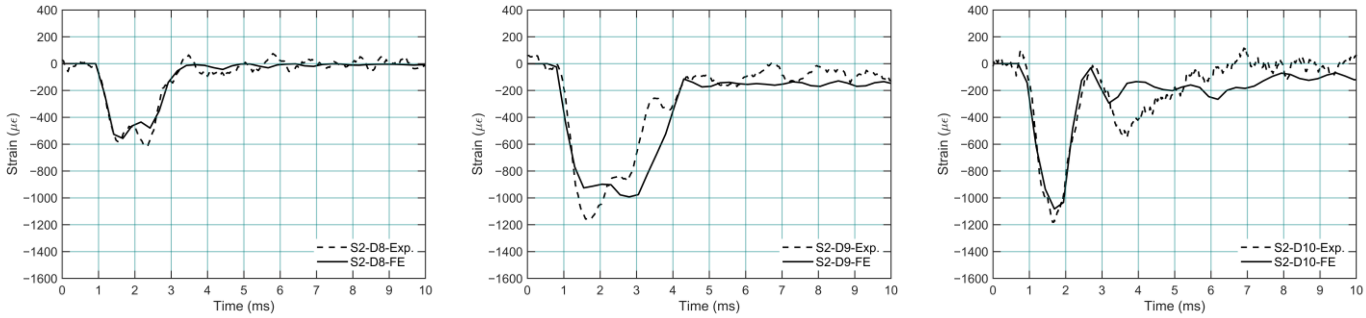

(**a**) (**b**) (**c**)

Figure 27. Strain–time histories of S2 for different drops: (**a**) eighth drop; (**b**) ninth drop; (**c**) tenth drop.

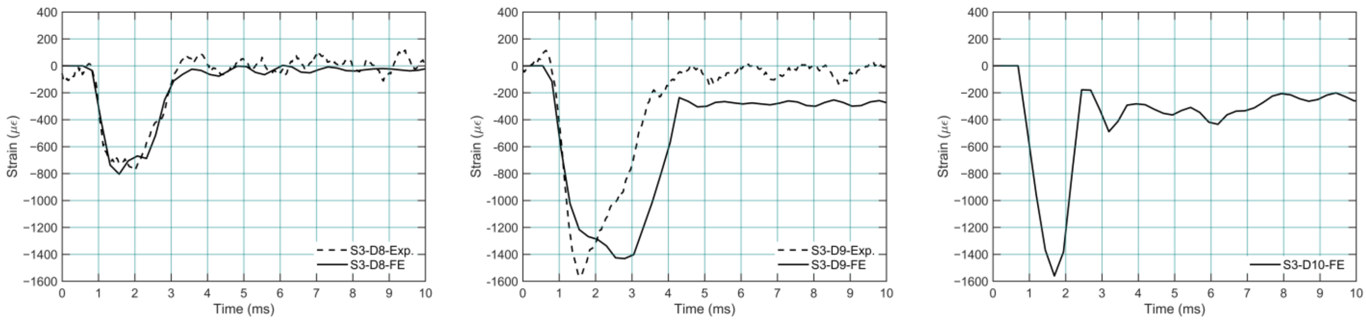

(**a**) (**b**) (**c**)

Figure 28. Strain–time histories of S3 for different drops: (**a**) eighth drop; (**b**) ninth drop; (**c**) tenth drop.

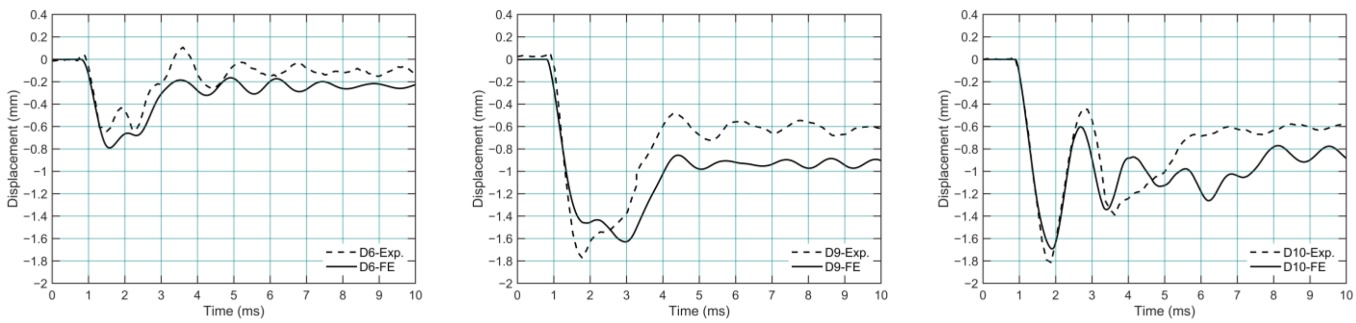

(**a**) (**b**) (**c**)

Figure 29. Displacement–time histories at A3 for different drops: (**a**) sixth drop; (**b**) ninth drop; (**c**) tenth drop.

The simulated acceleration–time histories at A3 showed good agreement with the experimental data in terms of overall waveform and timing of peaks (Figure 30). However, the model consistently predicted higher peak accelerations than in tests (Table 6), indicating a lower experimental momentum change rate. This discrepancy is likely due to one or more unmodelled effects: slight impactor inclination, energy absorption within the test rig, and rough contact at the plate surface that crushes asperities and delays momentum transfer [3].

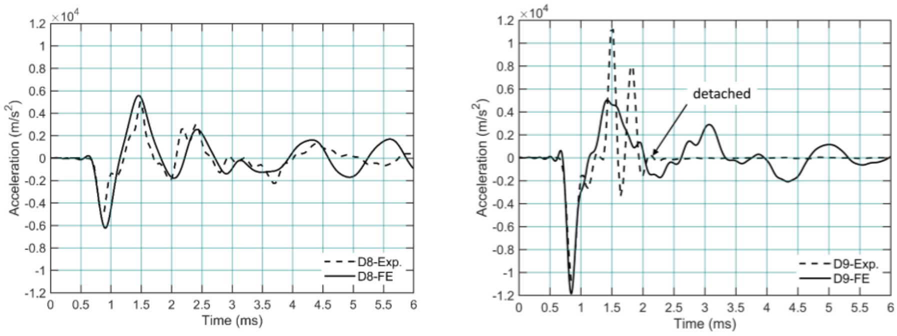

(**a**) (**b**) (**c**)

Figure 30. Acceleration–time histories at A3 for different drops: (**a**) eighth drop; (**b**) ninth drop; (**c**) tenth drop.

Table 6. Comparison of peak values in the numerical simulations and the experimental tests.

Drop No.	Acceleration at A3 (m/s2)			Displacement at A3 (mm)			Strain at SG2 (με)			Strain at SG3 (με)			Rebound Velocity (m/s)		
	Exp.	FE	Ratio *	Exp.	FE	Ratio *	Exp.	FE	Ratio *	Exp.	FE	Ratio *	Exp.	FE	Ratio *
8	5280	6282	1.19	0.63 †	0.818†	1.30	615	620	1.01	777	778	1.00	2.07	1.72	0.83
9	10,661	11,853	1.11	1.77	1.629	0.92	1157	992	0.86	1550	1431	0.92	2.17	1.97	0.91
10	7381	9500	1.29	1.81	1.692	0.93	1181	1082	0.92	NA	1560	NA	1.02	1.31	1.28

* Ratio = FE/Exp. NA: the strain gauge SG3 was destroyed by the crater formed during the 10th drop and no valid reading was obtained. † The sixth drop data were used.

The simulated rebound velocities for the eighth, ninth, and tenth drops were 1.72 m/s, 1.97 m/s, and 1.31 m/s, differing from tests by 16.9%, 9.2%, and 28.4%, respectively (Figure 31). The larger deviation in the 10th drop is attributed to the complex penetration and non-ideal impact conditions that are difficult to fully capture in the simulation.

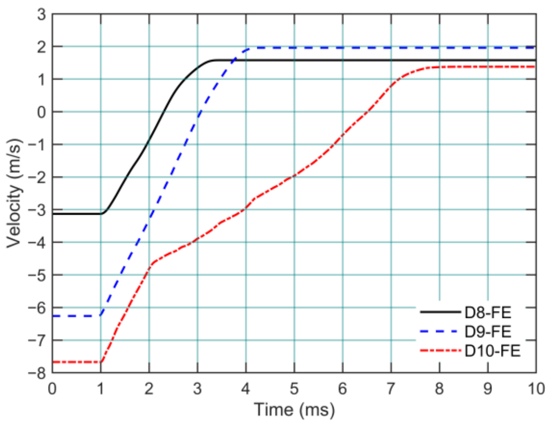

Figure 31. Velocities of impactor.

Beyond time histories of responses, the numerical model also demonstrated predictive capability in terms of damage pattern. As shown in Figure 32, the predicted tensile and compressive damage contours (dt, dc) after the 10th drop closely match the experimentally observed failure patterns (Figure 33). The simulation correctly predicted a central indentation (compressive damage) on the top surface and a combination of radial flexural cracks and a distinct circumferential crack (tensile damage) on the bottom surface, confirming the mixed flexural punching shear failure mode.

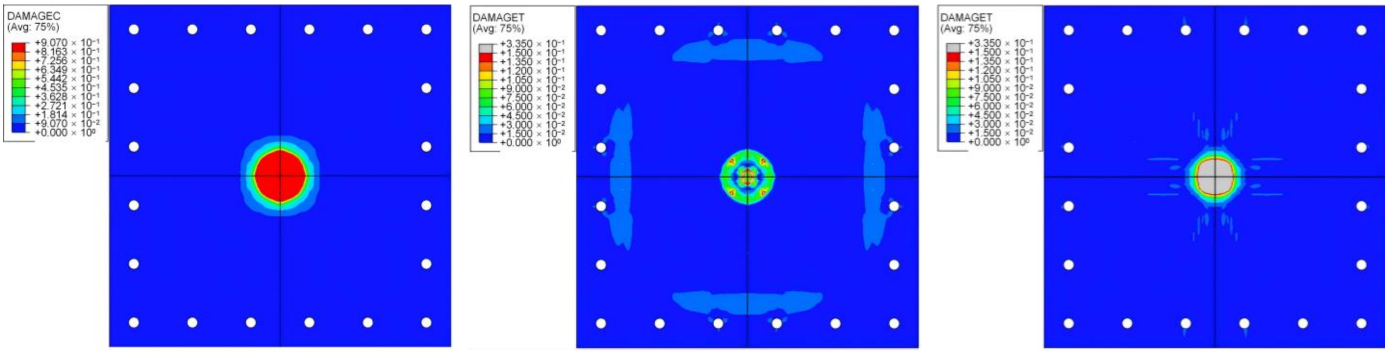

(**a**) (**b**) (**c**)

Figure 32. FE Damage contour of the plate following the 10th drop: (**a**) compressive damage (the top surface); (**b**) tensile damage (the top surface); (**c**) tensile damage (the bottom surface).

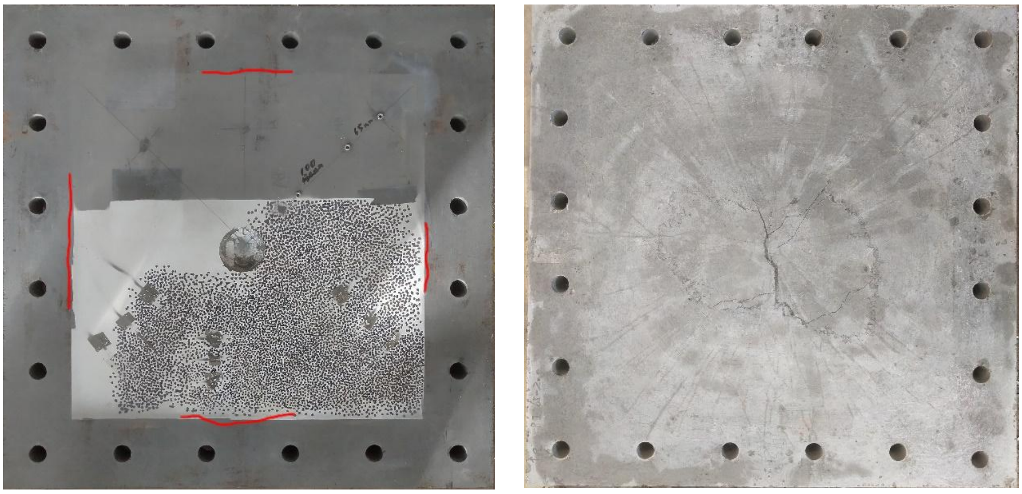

(**a**) (**b**)

Figure 33. Damages to the plate following the 10th drop: (**a**) top surface of the plate; (**b**) bottom surface of the plate. Red lines indicate cracks.

Although the CDP model does not directly visualize cracks, their orientation can be inferred from the direction of the principal plastic strains. The evolution of these strains on the plate's bottom surface was tracked by vector plots in the outermost bottom elements across multiple impacts (Figure 34). The simulation showed that the initial low-energy drop (first) induced small, circumferentially oriented plastic strains, corresponding to the formation of radial micro-cracks. Under the repeated 0.5 m drops, the model predicted a gradual accumulation of damage and a progressive rotation of the plastic-strain vectors out of the plane of the plate. Both quantities stabilized by the seventh drop, indicating that a steady state was reached at this energy level. This indicated the initiation of localized shear inclination beneath the impactor—a microscopic precursor that precedes, but does not constitute, the macroscopic failure mode. For clarity, the following criteria are adopted throughout this paper: flexural damage is identified by radial cracks, global deflection, and a stable or rising second force peak. Punching shear is instead identified by circumferential cracks, local penetration, attenuation of the transmitted dynamic response and a pronounced reduction of the second force peak accompanied by an energy absorption ratio approaching 100% (Table 4). At the higher drop heights of 2.0 m and 3.0 m, the plastic strain localizes into a conical band beneath the impactor, culminating in the predicted punching shear failure. This detailed analysis confirms the model's ability not only to predict the final failure mode but also to capture the underlying mechanics of damage progression.

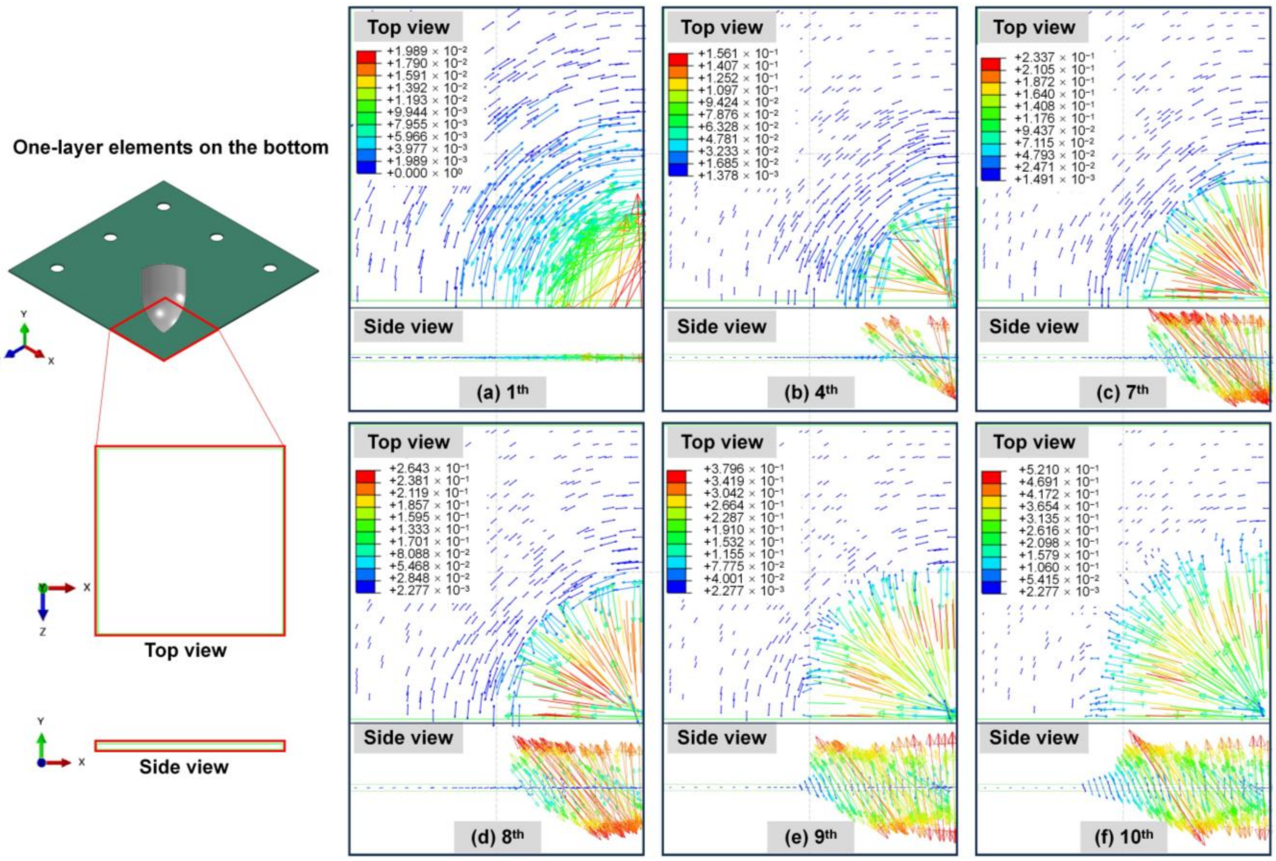

Figure 34. Vector symbol plot of maximum principal plastic strain (abs).

Overall, despite minor quantitative discrepancies attributable to experimental idealizations, the FE model provides a representation of the UHPFRC plate's dynamic response, damage evolution, and ultimate failure mode under repeated impact loading. As this agreement was achieved across three distinct energy levels against five independent response metrics (strain, acceleration, displacement, rebound velocity, and damage pattern), the results also provide indirect evidence of the robustness of the adopted parameter set. A dedicated parametric study on the CDP parameters is identified as future work in Section 5.4. Accordingly, the numerical conclusions are specific to the adopted parameter set and boundary representation for the investigated case, and their transferability to other configurations requires the parametric studies identified in Section 5.4.

4.4. Characteristics of Impact Force–Time Histories Under Repeated Impact

Having evaluated the FE model against the test data, it was employed to analyze the impact force–time histories, a parameter not directly measured in the experiments. The impact force, derived from the impactor's mass and simulated acceleration, provides critical insights into the plate's evolving resistance and failure mechanisms. For each of the eighth, ninth, and tenth drops, force–time histories were plotted alongside top-center, bottom-center, and A3-point displacements (Figure 35), revealing a consistent four-stage sequence within a single impact event: Stage I: Initial impulse. Upon contact, the impact force rises rapidly to a first peak (Point B), which is governed primarily by inertia and local contact stiffness rather than the plate's global structural resistance.

Hereafter, the model-derived peak resisting force (i.e., the resultant contact force extracted from the finite element model, which was not measured directly in the tests) refers to the second-peak force of Stage II, which is associated with the global structural resistance of the plate, as distinct from this initial inertial peak. Stage II: Global Deflection. After the initial impulse, the impactor continues to deflect the plate, transferring momentum and elevating the plate's kinetic energy. This leads to a temporary drop in force (Point C) and subsequent contact oscillations (segment CD). The majority of the impact energy is dissipated through global and local deformation during this stage. This stage ends at maximum center displacement. Stage III: Rebound. Stored elastic energy in the plate is released, pushing the impactor upward until separation occurs and the force returns to zero (Point E). In the case of a punching shear failure (e.g., the 10th drop), this stage is characterized by low force and penetration rather than a clean rebound (Figure 35c). Stage IV: Free vibration. After separation, the plate undergoes free vibration around its final equilibrium position, eventually settling at a state of permanent deformation.

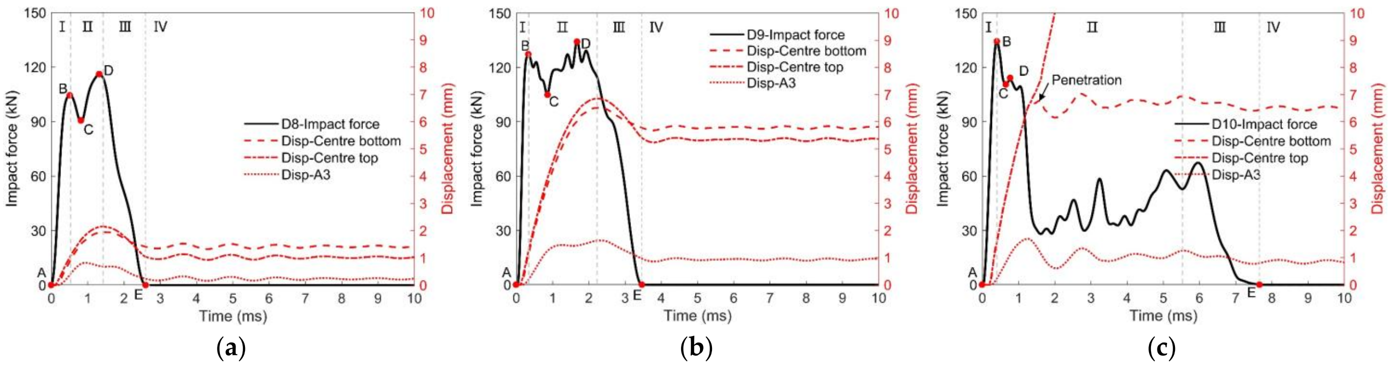

Figure 35. Impact force–time and displacement–time histories from FE simulation for (**a**) eighth drop; (**b**) ninth drop; (**c**) tenth drop.

The aforementioned four-stage sequence generally applies to all impact drops (Figure 35), but with distinct evolutionary trends:

- **Repeated low-energy impact (first to eighth, 0.5 m)**. The impact force history consistently exhibited two peaks, with the second peak being larger (Figure 36a). A slight decrease in peak force was observed with each successive impact, consistent with findings by Ranade et al. [3]. Despite this minor softening, the plate's peak resisting force remained stable in the range of 116–123 kN, indicating that the accumulated flexural damage was not yet critical.
- **Higher-energy impact (ninth drop, 2.0 m)**. The two-peak pattern persisted, but the second peak increased to 134 kN (Figure 36b). This demonstrates the plate's ability to resist the higher impact energy, reaching the highest global resisting force (134 kN, a model-derived quantity) observed in the investigated sequence.
- **Highest drop (tenth, 3.0 m)**. A critical shift in behavior was observed. The impact force history showed a prominent first peak followed by a much smaller second peak of only 113 kN. This substantial reduction in the peak resisting force, despite the higher impact energy than in the ninth drop, is one of several consistent indicators of the exhaustion of the plate's global resistance. This reduction is consistent with the transition to a lower-resistance punching shear failure mode under the investigated

loading sequence. This interpretation is corroborated by the damage evolution indices in Table 4: the energy absorption ratio reached approximately 98% in the 10th drop, confirming that nearly all the incident energy was dissipated within the localized punching zone, consistent with the negligible increase in global deflection predicted by the model over the same interval of the plate.

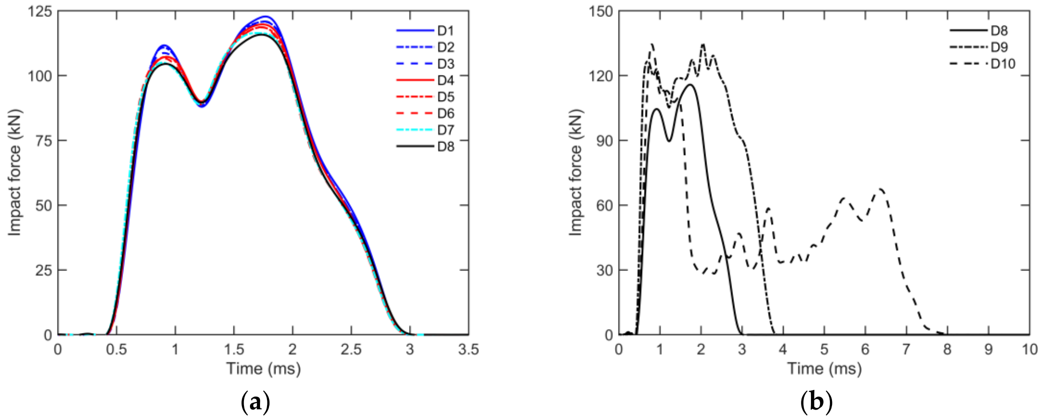

Figure 36. Impact force–time histories from FE simulation: (**a**) drops 1 to 8 (drops from 0.5 m); (**b**) drops 8 to 10.

5. Discussion

5.1. Comparison with Previous Studies

The damage progression observed in this study is consistent with, and extends, the findings of previous repeated impact studies on UHPC members. The flexural-to-punching transition and the associated reduction in peak resisting force agree with the behavior reported by Ranade et al. [3] for simply supported slabs, and the stable restitution response during the low-energy drops is in line with the superior damage tolerance of UHPFRC over HSC reported by Othman and Marzouk [7]. The present study extends these observations in three aspects: (i) the cumulative degradation was measured directly through 3D-DIC over a quarter field and reconstructed to the full field, rather than inferred from discrete quantities; (ii) quantitatively, the energy absorption ratio increased from approximately 56% to 98% across the loading sequence (Table 4), providing an energy-based characterization of the flexural-to-punching transition for a nominally fixed UHPFRC plate under a cumulative low-velocity impact sequence, tracked continuously from the undamaged state to local failure with a single, unchanged set of constitutive parameters; and (iii) the sequential FE strategy reproduced the entire damage accumulation process across ten impacts, whereas previous simulations were limited to single-impact events [3,31–33]. These aspects delineate the specific contribution of the present study; their applicability ranges and remaining gaps are discussed in Section 5.3.

5.2. Practical Engineering Implications

The findings of this study offer several implications for the design and assessment of protective structural components. First, the energy absorption ratio and residual central displacement derived in Section 3.4 and Section 3.6 constitute simple, experimentally accessible indices for quantifying the residual condition of an impacted plate. In practice, they could support post-event inspection and response-based condition assessment of protective slabs without dismantling, although a quantitative relationship with the actual residual capacity remains to be established through post-impact static loading tests. Second, the four-stage decomposition of the impact force history (Section 4.4) provides a diagnostic framework: a stable or rising second force peak indicates a structurally integral, flexure-dominated response, whereas a pronounced reduction of the second peak under a higher-energy impact signals the exhaustion of the flexural resistance and the transition to punching shear. This signature can guide the interpretation of instrumented impact tests in engineering applications where direct damage observation is impractical. Third, the 50 mm UHPFRC plate sustained seven repeated 196 J impacts, corresponding to a cumulative incident energy of 1372 J, without visible damage; the first visible indentation and the first micro-cracks appeared at the eighth impact of the same energy. This indicates that, for the configuration tested, the damage threshold is governed by the accumulated rather than the individual impact energy and that a design check based on a single impact event may be unconservative for similar components subjected to repeated service impacts, a hypothesis that requires verification using replicate testing.

5.3. Limitations

Several limitations of the present study should be acknowledged. (i) The impact program was conducted on a single plate following one prescribed loading sequence; the present work is accordingly framed as a detailed case study, in which specimen-to-specimen variability could not be assessed and the conclusions are strictly limited to the investigated sequence. (ii) The bolted clamping system provides a nominally fixed boundary; edge rotation, slip, and the actual bolt preload were not independently verified during impact. (iii) The impact force histories discussed in Section 4.4 are model-derived quantities, as the impactor was not instrumented; they should be interpreted as model-derived predictions evaluated against the measured structural responses, rather than direct measurements. (iv) The full-field displacement was reconstructed from quarter-plate DIC measurements assuming symmetry, any localized asymmetric deformation in severely damaged states may therefore not have been captured. (v) The UHPFRC was modelled as isotropic, whereas the radial casting flow may induce preferential fiber alignment; a tensile-only DIF with a ceiling of 10 s^{-1} was adopted, and compression rate enhancement was neglected within the present rate range. (vi) The impactor rebound velocity was estimated from the interval between acceleration peaks under a free-motion assumption, which may be biased by guide friction, repeated contact, impactor tilt and penetration. Although the stable estimates across identical drops (COV ≈ 0.5%) and the agreement with the FE predictions (within 9.2–28.4%) support its use for relative comparison, independent validation of the method was not available in this study. (vii) Modal indicators of stiffness degradation could not be extracted reliably from the present records because the free-vibration segment was truncated by the rebound and re-contact of the impactor. Direct modal identification before and after each impact is recommended in future programs. (viii) No post-impact static loading or remaining-strength test was performed; the proposed indices therefore characterize the damage state and the impact response rather than the actual residual capacity of the plate.

5.4. Future Research

Future work should include replicate specimens and independent single high-energy impacts on undamaged plates to separate the effects of impact energy from prior damage accumulation; instrumented impactors or load cells to directly validate the simulated force histories; systematic parametric studies on CDP parameters, boundary stiffness, and bolt preload; and refined constitutive descriptions accounting for casting-induced fiber orientation. Extending the sequential impact framework to plates of varying thickness and fiber dosage would further support the development of design-oriented residual capacity models.

6. Conclusions

This study presented an integrated experimental and numerical investigation into the progressive damage of a 50 mm thick, nominally fixed UHPFRC plate under repeated low-velocity impacts. A custom drop-weight test rig, coupled with high-speed 3D Digital Image Correlation (DIC), provided time-resolved, symmetry-reconstructed full-field data that served as a quantitative benchmark for evaluating a finite element (FE) model employing the CDP model. Within the limitations identified in Section 5.3, the following conclusions are drawn:

(1) The customized rig and stereo DIC delivered repeatable dynamics for the low-energy drops, and the quarter-plate DIC fields were verified as representative of the full plate and consistent with the accelerometer and strain-gauge records, providing a consistent basis for the reconstructed full-field analysis.

(2) The damage progressed in three distinct stages: negligible macroscopic damage under the repeated 0.5 m impacts, flexure-dominated cracking under the 2.0 m drop, and punching-dominated local failure under the 3.0 m drop with nearly complete energy absorption. Consistently, the model-assisted nominal secant stiffness indicator decreased gradually under the repeated low-energy drops, fell by approximately one half after the 2.0 m drop—marking the onset of the flexural-to-punching transition—and then stabilized, indicating that the additional incident energy was consumed mainly by local penetration rather than global flexure; this abrupt step additionally reflects the change in energy level and deformation mechanism at the ninth drop.

(3) The FE model incorporating the concrete damaged plasticity model was evaluated against the measured acceleration, strain and displacement (model-to-test ratios of 0.86–1.30) and the observed damage patterns. It successfully reproduced the transition from flexure to punching shear and proved useful for extracting quantities that were not directly measurable. Most notably, the impact force–time history was extracted in this way, and it accordingly remains a model-derived quantity.

(4) The model-derived impact force histories showed a stable peak resisting force during the low-energy impacts, a maximum at the 2.0 m drop, and a marked reduction at the 3.0 m drop despite the higher impact energy. This reduction is consistent with the experimentally observed transition to localized punching-dominated behavior under the investigated loading sequence.

(5) Two techniques proved valuable in this study. First, an energy-based definition of the CDP damage parameters, reproduced the stiffness degradation under repeated impacts for the investigated case. Second, a surface-fitting procedure reconstructed the complete plate deformation field despite impactor shadowing.

In summary, this study contributes to the theoretical basis of UHPFRC as a protective material by providing an experimentally grounded description of how cumulative damage governs the transition from flexural to punching shear failure under nominally fixed boundaries, together with an energy-based damage definition for repeated impact simulation. For engineering practice, it offers simple, measurable damage evolution indices and a diagnostic force-history framework that can support the response-based condition assessment of protective components in service. Future research will extend this framework toward replicate testing, instrumented impactors, and design-oriented residual capacity models, as outlined in Section 5.4. All findings and indices reported above are specific to the tested plate and the investigated loading sequence; the broader design implications are offered as hypotheses requiring verification through replicate testing.

Author Contributions: Conceptualization, Y.H., E.E., and M.S.; methodology, Y.H., E.E., and M.S.; software, Y.H. and E.E.; validation, Y.H., E.E., and A.J.; formal analysis, Y.H. and E.E.; investigation, Y.H.; resources, E.E., M.S., and J.-F.C.; data curation, Y.H.; writing—original draft preparation, Y.H. and E.E.; writing—review and editing, E.E., M.S., J.-F.C., and A.J.; visualization, Y.H., E.E., and A.J.; supervision, M.S. and J.-F.C.; project administration, M.S.; funding acquisition, M.S. All authors have read and agreed to the published version of the manuscript.

Funding: This research was funded by the Research Start-up Project of Xinjiang University, the PhD financial support provided by Xinjiang Uygur Autonomous Region Educational Commission and Xinjiang University from China, the H2020-MSCA-IF-2016 Grant (No. 753903), and the National Natural Science Foundation of China (No. 52178218).

Data Availability Statement: The datasets generated in this study, including the raw accelerometer and strain-gauge records, the DIC processing settings and the processed reconstructed full-field displacement data, the constitutive input curves, the Abaqus input files, and the MATLAB scripts used for the polynomial surface fitting, are available from the corresponding author upon reasonable request.

Acknowledgments: The authors are very grateful to the School of Natural and Built Environment (SNBE), Queen's University Belfast, for the facilities and the technical support that was provided during the experimental program of work. The high-speed cameras and technical help provided by James Nixon from the School of Mechanical and Aerospace Engineering, Queen's University Belfast, are highly acknowledged. The drop hammer test rig was fabricated with financial support from the Cyprus Research Promotion Foundation—Framework Programme for Research, Technological Development and Innovation 2009-10.

Conflicts of Interest: The authors declare no conflicts of interest. The funders had no role in the design of the study; in the collection, analyses, or interpretation of data; in the writing of the manuscript; or in the decision to publish the results.

Abbreviations

The following abbreviations are used in this manuscript:

UHPFRC	Ultra-high-performance fiber-reinforced concrete
FRP	Fiber reinforced polymer
HSC	High-strength concrete
GGBS	Ground granulated blast furnace slag
MSS	Microsilica slurry
SP	Superplasticizer
FE	Finite element
DIC	Digital image correlation
TPB	Three-point bending
IA	Inverse analysis
CMOD	Crack mouth opening displacement
DAQ	Data acquisition
FOV	Field of view
CDP	Concrete damaged plasticity
DIF	Dynamic increase factor

References

1. Dey, V.; Bonakdar, A.; Mobasher, B. Low-Velocity Flexural Impact Response of Fiber-Reinforced Aerated Concrete. *Cem. Concr. Compos.* **2014**, *49*, 100–110. https://doi.org/10.1016/j.cemconcomp.2013.12.006.
2. Micallef, K. The Dynamic Response of Blast-Loaded Monolithic and Composite Plated Structures. Doctoral Dissertation, Imperial College London, London, UK, 2013.

3. Ranade, R.; Li, V.C.; Heard, W.F.; Williams, B.A. Impact Resistance of High Strength-High Ductility Concrete. *Cem. Concr. Res.* **2017**, *98*, 24–35. https://doi.org/10.1016/j.cemconres.2017.03.013.
4. Gholipour, G.; Muntasir Billah, A.H.M. Numerical Investigation on the Dynamic Behavior of UHPFRC Strengthened Rocking Concrete Bridge Piers Subjected to Vehicle Collision. *Eng. Struct.* **2023**, *288*, 116241. https://doi.org/10.1016/j.engstruct.2023.116241.
5. Buchan, P.A.; Chen, J.F. Blast Resistance of FRP Composites and Polymer Strengthened Concrete and Masonry Structures–a State-of-the-Art Review. *Compos. Part B* **2007**, *38*, 509–522. https://doi.org/10.1016/j.compositesb.2006.07.009.
6. Wu, C.; Oehlers, D.J.; Rebentrost, M.; Leach, J.; Whittaker, A.S. Blast Testing of Ultra-High Performance Fibre and FRP-Retrofitted Concrete Slabs. *Eng. Struct.* **2009**, *31*, 2060–2069. https://doi.org/10.1016/j.engstruct.2009.03.020.
7. Othman, H.; Marzouk, H. Dynamic Identification of Damage Control Characteristics of Ultra-High Performance Fiber Reinforced Concrete. *Constr. Build. Mater.* **2017**, *157*, 899–908. https://doi.org/10.1016/j.conbuildmat.2017.09.169.
8. Sun, L.; Liu, S.; Zhao, H.; Muhammad, U.; Chen, D.; Li, W. Dynamic Performance of Fiber-Reinforced Ultra-High Toughness Cementitious Composites: A Comprehensive Review from Materials to Structural Applications. *Eng. Struct.* **2024**, *317*, 118647. https://doi.org/10.1016/j.engstruct.2024.118647.
9. Wei, J.; Li, J.; Liu, Z.; Wu, C.; Liu, J. Behaviour of Hybrid Polypropylene and Steel Fibre Reinforced Ultra-High Performance Concrete Beams against Single and Repeated Impact Loading. *Structures* **2023**, *55*, 324–337. https://doi.org/10.1016/j.istruc.2023.06.036.
10. Jafari, A.; Shahmansouri, A.A.; Bengar, H.A.; Zhou, Y. Flexural Rigidity of SFRC Columns at the Onset of Buckling Failure: Analytical and Numerical Study. *Steel Compos. Struct.* **2025**, *55*, 533–552. https://doi.org/10.12989/scs.2025.55.6.533.
11. Du, J.; Meng, W.; Khayat, K.H.; Bao, Y.; Guo, P.; Lyu, Z.; Abu-obeidah, A.; Nassif, H.; Wang, H. New Development of Ultra-High-Performance Concrete (UHPC). *Compos. Part B* **2021**, *224*, 109220. https://doi.org/10.1016/j.compositesb.2021.109220.
12. Bajaber, M.A.; Hakeem, I.Y. UHPC Evolution, Development, and Utilization in Construction: A Review. *J. Mater. Res. Technol.* **2021**, *10*, 1058–1074. https://doi.org/10.1016/j.jmrt.2020.12.051.
13. Yang, J.; Chen, B.; Su, J.; Xu, G.; Zhang, D.; Zhou, J. Effects of Fibers on the Mechanical Properties of UHPC: A Review. *J. Traffic Transp. Eng. (Engl. Ed.)* **2022**, *9*, 363–387. https://doi.org/10.1016/j.jtte.2022.05.001.
14. Xue, J.; Briseghella, B.; Huang, F.; Nuti, C.; Tabatabai, H.; Chen, B. Review of Ultra-High Performance Concrete and Its Application in Bridge Engineering. *Constr. Build. Mater.* **2020**, *260*, 119844. https://doi.org/10.1016/j.conbuildmat.2020.119844.
15. Zhu, Y.; Zhang, Y.; Hussein, H.H.; Chen, G. Flexural Strengthening of Reinforced Concrete Beams or Slabs Using Ultra-High Performance Concrete (UHPC): A State of the Art Review. *Eng. Struct.* **2020**, *205*, 110035. https://doi.org/10.1016/j.engstruct.2019.110035.
16. Huang, Y.; Grünewald, S.; Schlangen, E.; Luković, M. Strengthening of Concrete Structures with Ultra High Performance Fiber Reinforced Concrete (UHPFRC): A Critical Review. *Constr. Build. Mater.* **2022**, *336*, 127398. https://doi.org/10.1016/j.conbuildmat.2022.127398.
17. Yoo, D.-Y.; Banthia, N. Mechanical and Structural Behaviors of Ultra-High-Performance Fiber-Reinforced Concrete Subjected to Impact and Blast. *Constr. Build. Mater.* **2017**, *149*, 416–431. https://doi.org/10.1016/j.conbuildmat.2017.05.136.
18. Mao, L.; Barnett, S.J. Investigation of Toughness of Ultra High Performance Fibre Reinforced Concrete (UHPFRC) Beam under Impact Loading. *Int. J. Impact Eng.* **2017**, *99*, 26–38. https://doi.org/10.1016/j.ijimpeng.2016.09.014.
19. Musha, H.; Beppu, M. Impact Resistance Performance of UHPFRC Panels under Low Velocity Impact Loading. In Proceedings of the 3rd International Symposium on Ultra-High Performance Fibre-Reinforced Concrete (UHPFRC 2017), Montpellier, France, 2–4 October 2017; pp. 393–402.
20. Beppu, M.; Kataoka, S.; Ichino, H.; Musha, H. Failure Characteristics of UHPFRC Panels Subjected to Projectile Impact. *Compos. Part B* **2020**, *182*, 107505. https://doi.org/10.1016/j.compositesb.2019.107505.
21. Sovják, R.; Vavřiník, T.; Zatloukal, J.; Máca, P.; Mičunek, T.; Frydrýn, M. Resistance of Slim UHPFRC Targets to Projectile Impact Using In-Service Bullets. *Int. J. Impact Eng.* **2015**, *76*, 166–177. https://doi.org/10.1016/j.ijimpeng.2014.10.002.
22. Liu, J.; Wei, J.; Li, J.; Su, Y.; Wu, C. A Comprehensive Review of Ultra-High Performance Concrete (UHPC) Behaviour under Blast Loads. *Cem. Concr. Compos.* **2024**, *148*, 105449. https://doi.org/10.1016/j.cemconcomp.2024.105449.
23. Yin, X.; Li, Q.; Wang, Q.; Chen, B.; Xu, S. Near Range Explosion Resistance of UHPFRC Panels in Wide Scaled Distances: Experimental Study and Stochastic Numerical Modelling. *Int. J. Impact Eng.* **2024**, *192*, 105028. https://doi.org/10.1016/j.ijimpeng.2024.105028.

24. Farnam, Y.; Mohammadi, S.; Shekarchi, M. Experimental and Numerical Investigations of Low Velocity Impact Behavior of High-Performance Fiber-Reinforced Cement Based Composite. *Int. J. Impact Eng.* **2010**, *37*, 220–229. https://doi.org/10.1016/j.ijimpeng.2009.08.006.
25. Zaini, S.S. Impact Resistance of Pre-Damaged Ultra-High Performance Fibre Rreinforced Concrete Slabs. Doctoral Dissertation, University of Liverpool, Liverpool, England, 2015.
26. Khan, M.U.; Ahmad, S.; Al-Osta, M.A.; Algadhib, A.H.; Al-Gahtani, H.J. Effect of Fiber Content on the Performance of UHPC Slabs under Impact Loading–Experimental and Analytical Investigation. *Adv. Concr. Constr.* **2023**, *15*, 161–170. https://doi.org/10.12989/acc.2023.15.3.161.
27. Jia, P.C.; Wu, H.; Wang, R.; Fang, Q. Dynamic Responses of Reinforced Ultra-High Performance Concrete Members under Low-Velocity Lateral Impact. *Int. J. Impact Eng.* **2021**, *150*, 103818. https://doi.org/10.1016/j.ijimpeng.2021.103818.
28. Anil, Ö.; Kantar, E.; Yilmaz, M.C. Low Velocity Impact Behavior of RC Slabs with Different Support Types. *Constr. Build. Mater.* **2015**, *93*, 1078–1088. https://doi.org/10.1016/j.conbuildmat.2015.05.039.
29. Ekström, J. Blast and Impact Loaded Concrete Structures–Numerical and Experimental Methodologies for Reinforced Plain and Fibre Concrete Structures. Doctoral Dissertation, Chalmers University of Technology, Gothenburg, Sweden, 2017.
30. Jafarian Kafshgarkolaei, H.; Lotfollahi-Yaghin, M.A.; Mojtahedi, A. A Modified Orthonormal Polynomial Series Expansion Tailored to Thin Beams Undergoing Slamming Loads. *Ocean Eng.* **2019**, *182*, 38–47. https://doi.org/10.1016/j.oceaneng.2019.04.060.
31. Othman, H.; Marzouk, H. Applicability of Damage Plasticity Constitutive Model for Ultra-High Performance Fibre-Reinforced Concrete under Impact Loads. *Int. J. Impact Eng.* **2018**, *114*, 20–31. https://doi.org/10.1016/j.ijimpeng.2017.12.013.
32. Prem, P.R.; Verma, M.; Murthy, A.R.; Rajasankar, J.; Bharatkumar, B.H. Numerical and Theoretical Modelling of Low Velocity Impact on UHPC Panels. *Struct. Eng. Mech.* **2017**, *63*, 207–215.
33. Chun, B.; Ahn, H.; Cho, J.-Y.; Yoo, D.-Y. Enhancement of Flexural Performance of RC Slabs under Impact Loading Using Ultra-High-Performance Fiber-Reinforced Concrete. *J. Build. Eng.* **2025**, *111*, 113378. https://doi.org/10.1016/j.jobe.2025.113378.
34. Tiwari, V.; Sutton, M.A.; McNeill, S.R.; Xu, S.; Deng, X.; Fourney, W.L.; Bretall, D. Application of 3D Image Correlation for Full-Field Transient Plate Deformation Measurements during Blast Loading. *Int. J. Impact Eng.* **2009**, *36*, 862–874. https://doi.org/10.1016/j.ijimpeng.2008.09.010.
35. Baril, M.A.; Sorelli, L.; Réthoré, J.; Baby, F.; Toutlemonde, F.; Ferrara, L.; Bernardi, S.; Fafard, M. Effect of Casting Flow Defects on the Crack Propagation in UHPFRC Thin Slabs by Means of Stereovision Digital Image Correlation. *Constr. Build. Mater.* **2016**, *129*, 182–192. https://doi.org/10.1016/j.conbuildmat.2016.10.102.
36. Barnett, S.J.; Lataste, J.-F.; Soutsos, M.N. Assessment of Fibre Orientation in Ultra High Performance Fibre Reinforced Concrete and Its Effect on Flexural Strength. *Mater. Struct.* **2009**, *43*, 1009–1023. https://doi.org/10.1617/s11527-009-9562-3.
37. *ASTM C39/C39M-14*; Standard Test Method for Compressive Strength of Cylindrical Concrete Specimens. ASTM International, West Conshohocken, PA, USA, 2014.
38. Nicolaides, D.; Kanellopoulos, A.; Savva, P.; Petrou, M. Experimental Field Investigation of Impact and Blast Load Resistance of Ultra High Performance Fibre Reinforced Cementitious Composites (UHPFRCCs). *Constr. Build. Mater.* **2015**, *95*, 566–574. https://doi.org/10.1016/j.conbuildmat.2015.07.141.
39. Lane, B.; Sherratt, P.; Hu, X.; Harland, A. Measurement of Strain and Strain Rate during the Impact of Tennis Ball Cores. *Appl. Sci.* **2018**, *8*, 371. https://doi.org/10.3390/app8030371.
40. Wu, E.; Chang, L.-C. Woven Glass/Epoxy Laminates Subject to Projectile Impact. *Int. J. Impact Eng.* **1995**, *16*, 607–619. https://doi.org/10.1016/0734-743X(95)00001-Q.
41. Liu, K.; Zhao, J.; Wu, G.; Maksimenko, A.; Haque, A.; Zhang, Q.B. Dynamic Strength and Failure Modes of Sandstone under Biaxial Compression. *Int. J. Rock Mech. Min. Sci.* **2020**, *128*, 104260. https://doi.org/10.1016/j.ijrmms.2020.104260.
42. Yi, N.-H.; Kim, J.-H.J.; Han, T.-S.; Cho, Y.-G.; Lee, J.H. Blast-Resistant Characteristics of Ultra-High Strength Concrete and Reactive Powder Concrete. *Constr. Build. Mater.* **2012**, *28*, 694–707. https://doi.org/10.1016/j.conbuildmat.2011.09.014.
43. Mahmud, G.H.; Hassan, A.M.T.; Jones, S.W.; Schleyer, G.K. Experimental and Numerical Studies of Ultra High Performance Fibre Reinforced Concrete (UHPFRC) Two-Way Slabs. *Structures* **2021**, *29*, 1763–1778. https://doi.org/10.1016/j.istruc.2020.12.053.
44. Genikomsou, A.S.; Polak, M.A. Finite Element Analysis of Punching Shear of Concrete Slabs Using Damaged Plasticity Model in ABAQUS. *Eng. Struct.* **2015**, *98*, 38–48. https://doi.org/10.1016/j.engstruct.2015.04.016.
45. Sargin, M. Stress-Strain Relationship for Concrete and the Analysis of Structural Concrete Sections, Ph.D. Thesis, University of Waterloo, Waterloo, ON, Canada, 1968.
46. Liu, Z.; Chen, W.; Zhang, W.; Zhang, Y.; Lv, H. Complete Stress-Strain Behavior of Ecological Ultra-High-Performance Cementitious Composite under Uniaxial Compression. *ACI Mater. J.* **2017**, *115*, 783–794. https://doi.org/10.14359/51689899.

47. Bragov, A.M.; Petrov, Y.V.; Karihaloo, B.L.; Konstantinov, A.Y.; Lamzin, D.A.; Lomunov, A.K.; Smirnov, I.V. Dynamic Strengths and Toughness of an Ultra High Performance Fibre Reinforced Concrete. *Eng. Fract. Mech.* **2013**, *110*, 477–488. https://doi.org/10.1016/j.engfracmech.2012.12.019.
48. Thomas, R.J.; Sorensen, A.D. Review of Strain Rate Effects for UHPC in Tension. *Constr. Build. Mater.* **2017**, *153*, 846–856. https://doi.org/10.1016/j.conbuildmat.2017.07.168.
49. Chen, G.M.; Teng, J.G.; Chen, J.F.; Xiao, Q.G. Finite Element Modeling of Debonding Failures in FRP-Strengthened RC Beams: A Dynamic Approach. *Comput. Struct.* **2015**, *158*, 167–183. https://doi.org/10.1016/j.compstruc.2015.05.023.